JGR Solid Earth

RESEARCH ARTICLE
10.1029/2020JB021261

Key Points:

- Two synthetic salt-rocks are deformed in cyclic triaxial-compression to document interaction between pressure-dependent and pressure-independent micromechanisms at the brittle-plastic transition
- Semibrittle deformation involves coupled operation of grain-boundary crack opening, grain-boundary friction and water-assisted diffusional sliding, and intragranular dislocation glide
- Grain-boundary sliding by water-assisted diffusion leads to pronounced hysteresis and anelasticity at low strain rates

Correspondence to:
J. Ding,
jihuid@stanford.edu

Citation:
Ding, J., Chester, F. M., Chester, J. S., Shen, X., & Arson, C. (2021). Coupled brittle and viscous micromechanisms produce semibrittle flow, grain-boundary sliding, and anelasticity in salt-rock. *Journal of Geophysical Research: Solid Earth*, *126*, e2020JB021261. https://doi.org/10.1029/2020JB021261

Received 27 OCT 2020
Accepted 15 JAN 2021

Coupled Brittle and Viscous Micromechanisms Produce Semibrittle Flow, Grain-Boundary Sliding, and Anelasticity in Salt-Rock

J. Ding[1,2], F. M. Chester[1], J. S. Chester[1], X. Shen[3,4], and C. Arson[3]

[1]Center for Tectonophysics, Department of Geology & Geophysics, Texas A&M University, College Station, TX, USA, [2]Current address: Department of Geophysics, Stanford University, Stanford, CA, USA, [3]School of Civil and Environmental Engineering, Georgia Institute of Technology, Atlanta, GA, USA, [4]Current address: Department of Civil and Environmental Engineering, Northwestern University, Evanston, IL, USA

Abstract The operation of fracture, diffusion, and intracrystalline-plastic micromechanisms during semibrittle deformation of rock is directly relevant to understanding mechanical behavior across the brittle-plastic transition in the crust. An outstanding question is whether (1) the micromechanisms of semibrittle flow can be considered to operate independently, as represented in typical crustal strength profiles across the brittle to plastic transition, or (2) the micromechanisms are coupled such that the transition is represented by a distinct rheology with dependency on effective pressure, temperature, and strain rate. We employ triaxial stress-cycling experiments to investigate elastic-plastic and viscoelastic behaviors during semibrittle flow in two distinctly different monomineralic, polycrystalline, synthetic salt-rocks. During semibrittle flow at high differential stress, granular, low-porosity, work-hardened salt-rocks deform predominantly by grain-boundary sliding and wing-crack opening accompanied by minor intragranular dislocation glide. In contrast, fully annealed, near-zero porosity salt-rocks flow at lower differential stress by intragranular dislocation glide accompanied by grain-boundary sliding and opening. Grain-boundary sliding is frictional during semibrittle flow at higher strain rates, but the associated dispersal of water from fluid inclusions along boundaries can activate fluid-assisted diffusional sliding at lower strain rates. Changes in elastic properties with semibrittle flow largely reflect activation of sliding along closed grain boundaries. Observed microstructures, pronounced hysteresis and anelasticity during cyclic stressing after semibrittle flow, and stress relaxation behaviors indicate coupled operation of micromechanisms leading to a distinct rheology (hypothesis 2 above).

Plain Language Summary Controlled deformation experiments on rock are conducted to develop a general understanding of the mechanical properties of earth materials in the crust. Rock consists of an assemblage of mineral grains in tight contact and undergoes deformation in nature by operation of several microscopic processes that often operate simultaneously. When multiple processes occur, their interaction and combined effects can be complex. In this study, two synthetic salt-rocks are deformed under cyclic loading at pressures and rates that activate multiple microscopic processes. Recoverable and permanent deformations are measured during the experiments, and deformation features are studied using a microscope after experiments. Our findings document that linked networks of opening cracks along grain boundaries and of sliding cracks along grain boundaries is the main process of deformation; but, deformation inside grains and chemical reactions along grain boundaries with water also are important. We find that with small amount of water and low rates of deformation, the chemical action of water can strongly influence mechanical behavior. Our findings indicate that the interactions between multiple microscopic processes must be considered to describe the mechanical behavior of rock accurately.

1. Introduction

Rock deforms by a variety of microprocesses, including brittle processes of fracturing and frictional sliding that are strongly pressure-dependent, as well as viscoplastic processes of intracrystalline plasticity and diffusive mass transfer that are largely pressure-independent, but strongly temperature- and rate-dependent (Knipe, 1989; Sibson, 1977, 1986; Tullis, 1979). Semibrittle refers to deformation involving com-

bined operation of brittle and intracrystalline plastic micromechanisms and is generally relevant to the brittle-plastic transition with depth in the crust or mantle (Carter & Kirby, 1978; Chester, 1989; Paterson & Wong, 2005; Reber & Pec, 2018). Most commonly, the combined and concurrent operation of multiple distinct micromechanisms of deformation is treated as independent processes, that is the distinct mechanisms operate as parallel-concurrent and the total strain rate is the sum of that achieved by each mechanism. Viewing steady semibrittle flow in this way, a mechanical-analog diagram would consist of dashpots and slider blocks connected in series. Treatment of multiple microprocesses of deformation as independent is well illustrated by the classic deformation-mechanism maps of high temperature and pressure mechanisms involving intracrystalline plasticity and diffusion (e.g., Frost & Ashby, 1982), as well as in more recent work representing the brittle-plastic transition for brittle-creep to dislocation creep and dissolution-precipitation creep (Reber & Pec, 2018). Another example of treating deformation across the brittle-plastic transition in terms of independent mechanisms is the strength profiles constructed for the crust and lithosphere, where the brittle mechanisms are represented by a friction relation, and the plastic by relations for dislocation glide and dislocation creep (e.g., Brace & Kohlstedt, 1980; Kohlstedt et al., 1995; Sibson, 1983). In most strength profiles and deformation-mechanism maps, the brittle-plastic transition appears relatively abrupt and without a distinct representation of semibrittle deformation.

It is likely that in some cases, the micromechanisms operating concurrently during semibrittle flow are coupled and operate as series-sequential, such that a mechanical-analog diagram would consist of a dashpot and slider block connected in parallel. In this case, rock strength during semibrittle flow would be less than if the mechanisms were operating independently and would constitute a distinct mechanism field that is represented by a constitutive relation in which flow strength has both pressure, temperature, and strain-rate dependencies. An example of coupled interaction of brittle and viscous processes during semibrittle flow in quartz aggregates include the development of lattice preferred orientations in grains oriented for easy glide (basal and prism slip) while grain-scale faults and microcracks accommodate strain incompatibilities at grain boundaries associated with a limited number of independent slip systems (Hirth & Tullis, 1994). Under this mode of deformation, it is likely that the flow strength shows pressure dependence associated with the dilatant cracking, and rate and temperature dependence with intracrystalline plasticity, and the macroscopic behavior reflects series-sequential operation of the brittle and viscous mechanisms to achieve flow. More work is needed to elucidate how the combined operation of brittle and viscous microprocesses affects both elastic and inelastic deformation in the semibrittle regime, and whether the simultaneous operation of the different mechanisms is coupled or independent.

It is challenging to achieve pressure, temperature, and strain rate conditions in the laboratory that are needed to study the mechanical behavior of semibrittle flow of silicate rocks (e.g., Hirth & Tullis, 1994; Pec et al., 2012, 2016). In contrast, minerals such as calcite and halite deform by intracrystalline plastic and diffusion processes at room temperature, and semibrittle flow can be achieved more readily in experiments (Fredrich et al., 1989; Shimamoto, 1986). Synthetic salt-rock is often chosen to study deformation behaviors and microprocesses to develop micromechanical models (e.g., Spiers et al., 1990; Ter Heege et al., 2005). By varying fabrication conditions (e.g., temperature, stress) and mineral composition (e.g., halite, impurities), synthetic salt-rock can be engineered to allow well-targeted studies. Over the past 35 years, a fairly comprehensive study of the brittle to plastic transition, including the semibrittle field, has been carried out by deforming monomineralic, polycrystalline synthetic salt-rock in triaxial shear, direct shear, and rotary shear configurations. The shear experiments on synthetic salt-rock are viewed as analogs to faulting in other monomineralic or bi-mineralic, polycrystalline rocks in the crust and mantle (e.g., Bos & Spiers, 2002b; Chester, 1988a; Shimamoto, 1989). The shear configurations allow fairly large displacements and shear strain such that steady-strength flow can be achieved (Bos & Spiers, 2001; Bos et al., 2000a, 2000b; Chester, 1989; Chester & Logan, 1990; Noda & Takahashi, 2016; Shimamoto, 1986). Combined, the studies of sheared halite have documented the transition from brittle, frictional sliding to pressure-insensitive viscous flow by dislocation creep, and the marked dependence of flow strength on pressure, temperature, and strain rate within the semibrittle field. Empirical flow models can reproduce steady-state flow strength and transient rate-dependent behavior across the friction to viscous flow transition documented in the laboratory (Chester, 1988a, 1988b; Noda & Shimamoto, 2010, 2012; Shimamoto & Noda, 2014), but a micromechanical basis for describing the interaction of brittle and viscous mechanisms across the transition is lacking and deserves further study.

Semibrittle processes are directly relevant to deformation of the crust and upper mantle, and particularly to earthquake nucleation and rupture through the base of the seismogenic zone. Abundant microstructural evidence confirms a mixed mode of frictional and viscous microprocesses (Fusseis & Handy, 2008; Mancktelow & Pennacchioni, 2020; Melosh et al., 2018; Stewart et al., 2000; Wehrens et al., 2016; White & White, 1983; Zulauf, 2001), which are primarily controlled by lithology and environmental conditions of effective pressure and temperature. While confining pressure and temperature are considered relatively stable in the subsurface, the stress state, strain rate, and fluid pressure are expected to vary considerably over the seismic cycle (Ellis & Stöckhert, 2004; Ivins, 1996; Matysiak & Trepmann, 2012; Nüchter & Stöckhert, 2008; Scholz, 2019). Earthquake rupture propagation into the viscous regime, dramatically raising strain rate and possibly pore-fluid pressure, will impose an extension of brittle deformation to deeper levels and produce considerable changes in rock microstructure, crack porosity, and possible fluid migration. Such changes in rock structure and availability of water may activate transient elastic and inelastic behaviors that are poorly represented by steady-state flow laws or friction laws.

The purpose of this paper is to report an experimental and microstructural investigation of semibrittle deformation in salt-rocks aimed at understanding grain-scale micromechanisms of deformation and their interaction during steady plastic flow and cyclic elastic loading. We use reagent-grade, granular halite to fabricate two synthetic salt-rocks with contrasting microstructure (i.e., porosity, dislocation density, grain size, and shape). One of the salt-rocks is a granular, low porosity, work-hardened aggregate produced in the laboratory by uniaxial-strain consolidation at temperature. The "consolidated" sample contains significant water in the form of inter- and intragranular inclusions of brine and is considered qualitatively representative of a natural rock formed by a high strain-rate event (e.g., earthquake) within the semibrittle regime. The other salt-rock is produced by annealing of a mechanically consolidated aggregate to form a fully dense polycrystalline rock. The "annealed" sample contains only trace amounts of water as grain-boundary inclusions, and is considered qualitatively representative of a naturally deformed rock formed by dislocation creep or postdeformation annealing during low strain rate periods (e.g., interseismic). Both of the synthetic salt-rocks are deformed in triaxial compression using cyclic loading and stress-relaxation at room temperature and low confinement to achieve semibrittle flow, as well as to document time-dependent elastic behavior (viscoelastic, anelastic). By conducting the same types of experiments on two synthetic rocks with distinctly different starting microstructure and water content, we are able to document the coupled operation of deformation mechanisms that are likely relevant to natural deformation of monomineralic, polycrystalline rock in the semibrittle regime.

2. Methods

2.1. Fabrication of Two Synthetic Salt-Rocks

Reagent-grade granular salt (99 wt.% NaCl) was used to fabricate two distinct synthetic salt-rocks with contrasting microstructure: the "consolidated" and the "annealed" samples. The consolidated samples were fabricated through uniaxial consolidation of 0.3–0.355 mm diameter granular salt at a displacement rate of 0.34 mm/s, a temperature of 150°C, and a maximum axial stress of 75 MPa. Procedures for uniaxial consolidation can be found in Ding et al. (2016). The annealed samples were produced by uniaxial consolidation followed by annealing. The consolidation step was the same as used for the consolidated samples, except that consolidation temperature and maximum axial stress were changed to 100°C and 120 MPa, respectively. For annealing, the consolidated samples were sealed and placed in a pressure vessel at a temperature of 150°C and a hydrostatic pressure of 100 MPa for a duration of 1 week. Fabricated samples are right-circular cylinders (19 mm diameter and 43 mm length), so from measurements of dimensions and mass, the starting bulk porosity of consolidated and annealed samples were 5.45% ± 0.06% and 0.54% ± 0.08%, respectively. Based on image analysis of micrographs, consolidated and annealed samples have grain sizes of 0.273 ± 0.072 mm and 0.241 ± 0.146 mm, respectively. Although average grain size is similar, annealing produced wider grain size distribution.

The rheological behavior of salt-rock can be greatly influenced by the amount of water in sample (Urai et al., 1986; Watanabe & Peach, 2002). Using a Fourier transform infrared (FTIR) spectrometer (method described in (Ding, 2019), water contents of consolidated and annealed samples were determined as 301.22 ± 18.01 and 5.10 ± 0.44 ppm, respectively. To ensure consistency in water content after fabrication,

Table 1
Sample Classification and Experiments[a] Performed

Sample no.	Sample type	Final axial strain (%)	Test performed	Notes
60209R	Granular	N/A	N/A	Sectioned
70516	Consolidated	N/A	Undeformed	Sectioned
61003	Consolidated	2.77[b]	Cyclic loading	Sectioned
61123	Consolidated	7.31[b]	Cyclic loading	Sectioned
80204	Consolidated	8.79	Stress relaxation	Sectioned
80306	Consolidated	3.82	Cyclic loading, hold	First-round of cyclic loading
80306	Consolidated	3.79	Cyclic loading	Second-round of cyclic loading
61030	Annealed	N/A	Undeformed	Sectioned
70304	Annealed	4.87[b]	Cyclic loading	Sectioned
70305-2	Annealed	3.51	Cyclic loading, hold	First-round of cyclic loading
70305-2	Annealed	2.96	Cyclic loading, hold, stress relaxation	Second-round of cyclic loading

[a]All experiments were conducted at room temperature and a confining pressure of 1 MPa. [b]Final axial strains equivalent to strain gauge measurements were estimated based on total axial strains measured by an external DCDT and experiments with both strain gauge and DCDT strain measurements (i.e., sample 80306 and 70305-2).

samples were stored and handled in a controlled low-humidity glove-box where relative humidity was maintained below 17% (Ding et al., 2016). Qualitatively, the consolidated samples may be characterized as wet, whereas the annealed samples are dry (Watanabe & Peach, 2002). The contrasting microstructure and water content of the two synthetic salt-rocks allowed detailed study of microstructural control on the mechanical behavior.

2.2. Cyclic Triaxial Compression and Stress Relaxation Experiments

The tests were performed at room temperature and a confining pressure of 1 MPa (Table 1) to induce semibrittle deformation in a triaxial apparatus well suited for deformation experiments on weak geomaterials (Coble et al., 2014; French et al., 2015; Kitajima et al., 2012). While maintaining a constant confining pressure and using a constant axial displacement rate, the differential stress in the direction of sample axis was varied in two types of load cycles: (1) small-load cycles in which differential stress was cycled between 0 and ~6.5 MPa and the sample deformed elastically (i.e., deformation is reversible), and (2) large-load cycle in which differential stress was cycled between zero and the flow strength, and the sample was deformed permanently by a specified increment of axial shortening before the unload portion of the cycle (Figure 1). Except for those performed at zero axial strain, small-load cycles were started ~15 min after the preceding unload from flow strength was completed to ensure a consistent amount of rest time before initiating measurements of anelasticity (i.e., time-dependent elasticity) in all tests. This step reduced the impact of time-dependent deformation from large-load cycles on subsequent small-load cycles. A constant strain rate of 3×10^{-6} s^{-1} was used for large-load cycles, while three different strain rates of 3×10^{-5}, 3×10^{-6}, and 3×10^{-7} s^{-1} were used in small-load cycles to investigate the rate-dependence of anelastic behavior. Axial and radial strains were measured by two rosette strain gauges of 0.25-inch gauge length and 350 Ω resistance. Strain gauges were glued at opposing sides of the sample and averaged to account for sample tilting during deformation tests (Figure 2), although the differences in strain measurements of a sample is less than 0.006. Differential force was measured through a semi-internal force gauge that is in direct contact with sample assembly and unaffected by the friction between the loading piston and sealing stack. The differential force gauge and confining pressure are accurate to ±70 N, ±0.01 MPa, respectively. The triaxial deformation apparatus used in this study has been described in greater detail by French et al. (2015). Daily temperature variation of the apparatus during test period was less than 0.8°C.

To investigate the time dependence of changes in elastic properties, a "hold" was employed between two rounds of cyclic loading tests on the same sample. The salt-rock sample was first deformed to approxi-

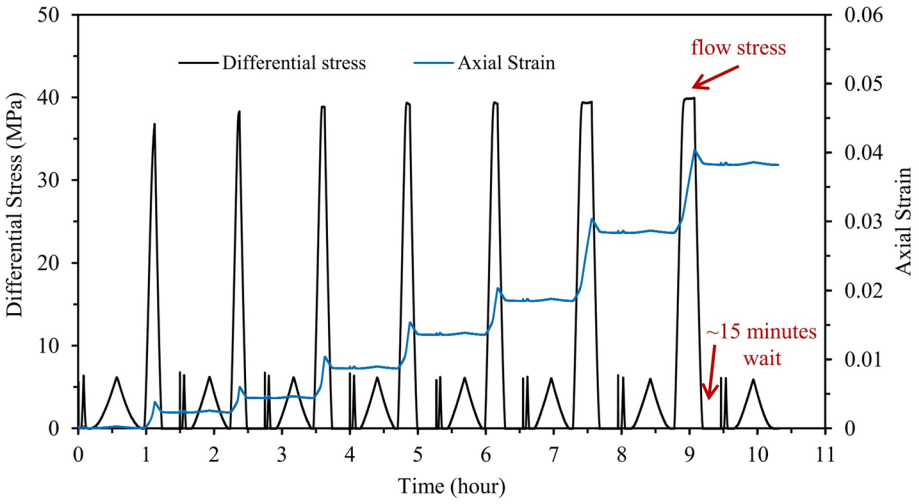

Figure 1. Differential stress and axial strain versus time for the first-round of cyclic triaxial compression test (sample 80306). Small-load cycles were applied before and after large-load cycles. A ~15-min wait was applied before small-load cycles that followed large-load cycles. A second-round of cyclic triaxial compression test was performed on this sample using the same load path. In between the two rounds of cyclic loading, the sample was on hold without load for 34.5 h. Flow stress refers to the differential stress at which the sample undergoes macroscopically ductile deformation.

mately 4% axial strain, close to the linear limit of the strain gauges (4.5%), to record the evolution of elastic properties with axial strain. Then the sample was removed from the vessel and the strain gauges were replaced, after which samples were held at either at 0 or 1 MPa confining pressure for a period of time (1–5 days). After the hold, a second-round of cyclic loading was performed on the sample following similar stress cycles as used in the first-round (Figure 1).

Stress relaxation tests also were conducted to gain more information on time-dependence and deformation mechanisms (Table 1). The loading piston was abruptly stopped when a sample was being deformed at a constant strain rate. Differential stress on the sample decreases with time as elastic energy stored in the sample and loading rig is converted into inelastic strain. The stress relaxation was continued until strain rate decreased to 1×10^{-9} s^{-1} or below at room temperature. Differential stress and axial strain were recorded. The stress relaxation technique allows determination of inelastic deformation mechanisms through the analysis of strain rate versus stress behavior (French et al., 2015; Rutter et al., 1978).

2.3. Microstructural Characterization

Loosely packed salt grains, the consolidated and annealed synthetic salt-rock samples, and key synthetic salt-rock samples deformed in triaxial compression, were epoxy-saturated, cut along the cylinder axis, and polished to make petrographic sections, and then chemically etched to allow observation of grain-scale features, including grain boundaries and dislocations (Table 1). All steps of cutting and polishing samples were carried out using the low-humidity glove-box. The sectioning and etching procedures follow the techniques developed by Spiers et al. (1986) with minor modifications. Microstructures were characterized under both reflected- and transmitted-light. Observations focus on the central part of the sample, near where the strain gauges were attached, for the benefit of direct correlation between microstructures and mechanical data as well as reduced sample end-effects. In addition to detailed observation on a few halite grains in a single photomicrograph of an area 1 mm^2 or smaller, tens of images were stitched together to allow observation of one to two hundred grains in an area of approximately 20 mm^2, which is equal to about 40% of the strain gauge area.

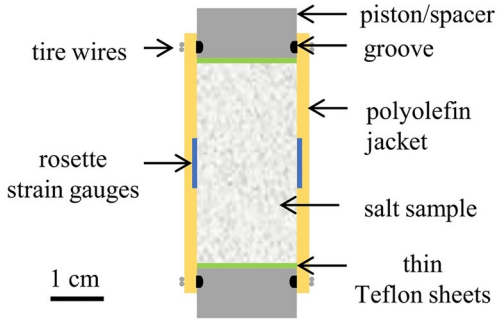

Figure 2. Schematic of sample assembly.

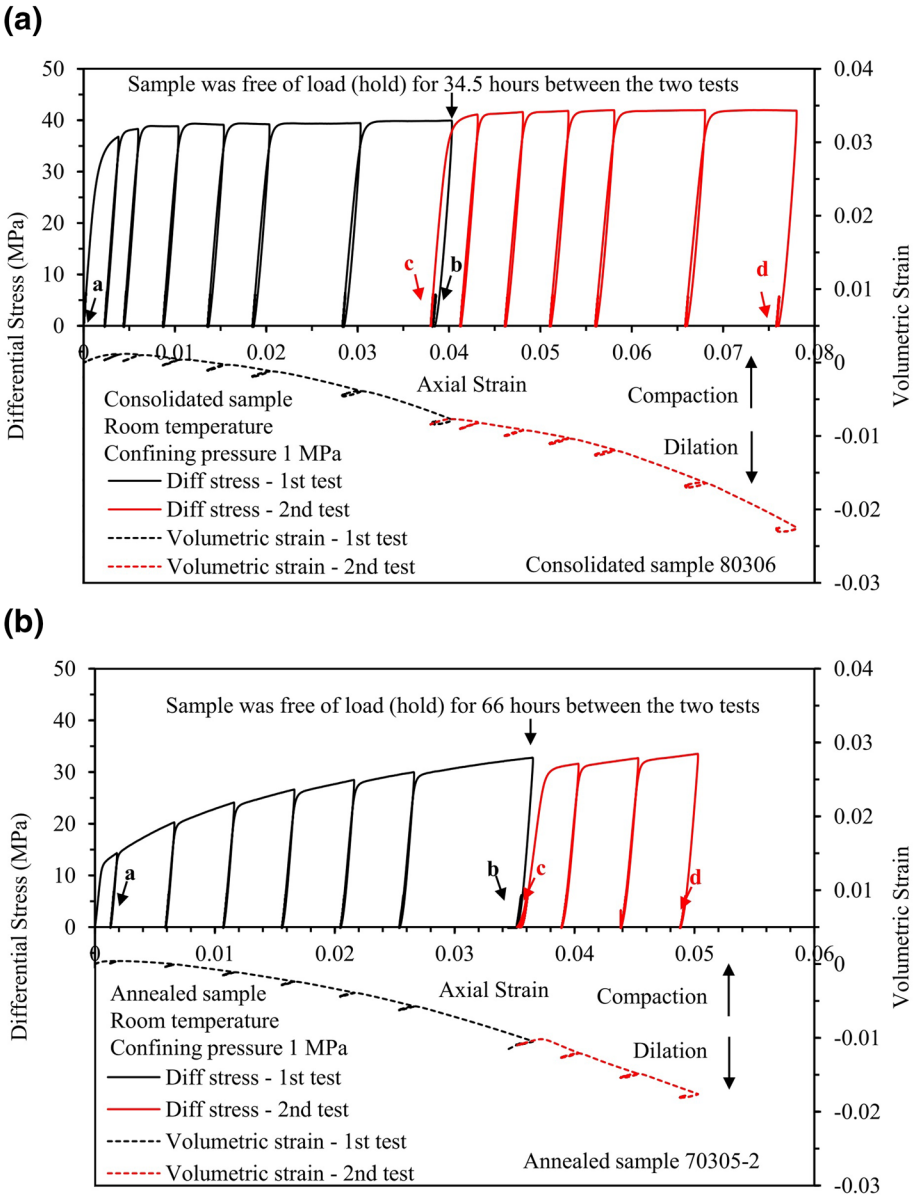

Figure 3. Plots of differential stress and volumetric strain versus axial strain for (a) consolidated sample 80306 and (b) annealed sample 70305-2. The first and last small-load cycles for each round of cyclic compression test are indicated by letters. Note small-load cycles are not readily seen due to scale and masking by large-load cycles.

3. Results

3.1. Mechanical Behavior

3.1.1. Overall Stress-Strain Behavior

At room temperature and a confining pressure of 1 MPa, the mechanical behavior of the consolidated samples is characterized by approximately linear elastic deformation, yielding at approximately 36 MPa, followed by inelastic deformation at relatively constant stress of ~40 MPa (Figure 3a). The inelastic deformation is homogeneous across the samples with only a slight barreling in the middle. In the beginning of the deformation experiment the sample compacts slightly and then steadily dilates thereafter, documenting a porosity increase. The semibrittle flow strength and rate of porosity increase for the two rounds of cyclic loading tests, separated by a 34.5 h hold without confinement, are highly consistent (Figure 3a). At the

same testing conditions used for the consolidated samples, the annealed samples show similar mechanical behavior except for yielding at lower stress (~13 MPa) and work-hardening at a progressively decreasing rate throughout the deformation test (Figure 3b). The final strength of the annealed samples is about 80% of the semibrittle flow strength of the consolidated samples. Dilatancy occurs at an increasing rate throughout the deformation test indicative of a net increase in porosity of about 2% in both annealed and consolidated samples. After the annealed sample undergoes an unconfined hold for 66 h, the second-round cyclic loading was initiated. The first loading cycle of the second-round shows apparent reduction in slope (Young's modulus) relative to earlier load cycles, likely from the presence of the microcracks developed from unloading sample (i.e., unloading cracks). After imposing ~0.5% inelastic axial strain during the first load cycle, the subsequent unload-load cycles show greater slopes of stress-strain curves comparable with those of the first-round of cyclic loading test, indicating the unloading cracks produced during the unconfined hold are effectively closed during the first large-load cycle of the second round.

3.1.2. Stress-Strain Behavior During Small-Load Cycles

Small-load cycles of consolidated samples exhibit characteristic stress-strain behavior (Figure 4). For the first-round of cyclic loading at zero axial strain, before the first large-cycle loading, samples show nearly perfect linear elastic deformation, and the subsequent small-load cycles of different strain rates overlie exactly (Figure 4a). As permanent axial strain increases with the large-load cycling, the elastic response during the small-load cycles progressively develops a nonlinear elastic response with hysteresis that is rate-dependent. Slower loading and unloading lead to more compliant behavior and hysteresis (Figure 4b); however, even with hysteresis, the axial strain is nearly fully recovered during a single small load-unload cycle regardless of strain rate, whereas radial strain recovers more than initially achieved. During the ~15 min between complete unload of large cycles and start of small cycles, appreciable axial and radial strain is recovered providing evidence of anelasticity consistent with the hysteresis and rate-dependence of elastic behavior seen in the small-load cycles (Figure 4b and 4d). For the second-round cyclic loading test, after the days-long hold with no confinement, the behavior during the first small-load cycle (which precedes the first large cycle) shows that the sample recovers to the initial state (i.e., the state prior to initiating the first-round of small-load cycling) where hysteresis and rate-dependence are absent (Figure 4c). With continued deformation, the sample displays the same evolution as in the first-round of cyclic loading before the hold, that is, increasing rate-dependence and hysteresis with permanent strain (Figure 4d).

The small-load cycles of annealed samples (Figure 5) show quite different stress-strain behavior from those of consolidated samples in that rate-dependence and hysteresis are largely absent throughout the deformation tests. Closing of unloading cracks is evident in the first small-load cycles of the second-round test (Figure 5c), but subsequent small-load cycles show similar stress-strain behaviors as those of the first-round test (Figure 5d). Very little axial and radial strain is recovered during the ~15 min between complete unload of large cycles and the start of small cycles (Figure 5b and 5d).

3.1.3. Young's Modulus and Poisson's Ratio

Young's modulus and Poisson's ratio are determined for loading and unloading using best-fit linear relation over the stress intervals of 2.5–5.5 MPa for small cycles, and stress intervals of 18–21 MPa for large cycles. Observed modulus and Poisson's ratio from small and large stress cycles show similar evolution in magnitude with permanent strain. Accordingly, only the Young's modulus and Poisson's ratio determined from the loading interval of the small-load cycles are presented (Figure 6). The differential stress range used in linear fitting covers a major part of the stress cycling of small-load cycles (between 0 and 6.5 MPa) and therefore reflects the overall slope well. As shown in the previous section, axial strain is nearly fully recovered during small-load cycles even when there is appreciable hysteresis. Therefore, the stress-strain behavior of small-load cycles is considered elastic.

For consolidated samples, Young's modulus of small-load cycles shows clear evolution with inelastic deformation (Figure 6a). Overall, for the first-round of cyclic loading, Young's modulus decreases with increasing inelastic deformation. At zero axial strain, Young's modulus at different loading rates are similar, but as inelastic deformation increases, they progressively diverge in magnitude. After the days-long hold, in the first set of small-load cycles of the second-round tests, the Young's modulus is nearly the same as the original values at zero axial strain and are similarly rate-insensitive. With further permanent strain in the

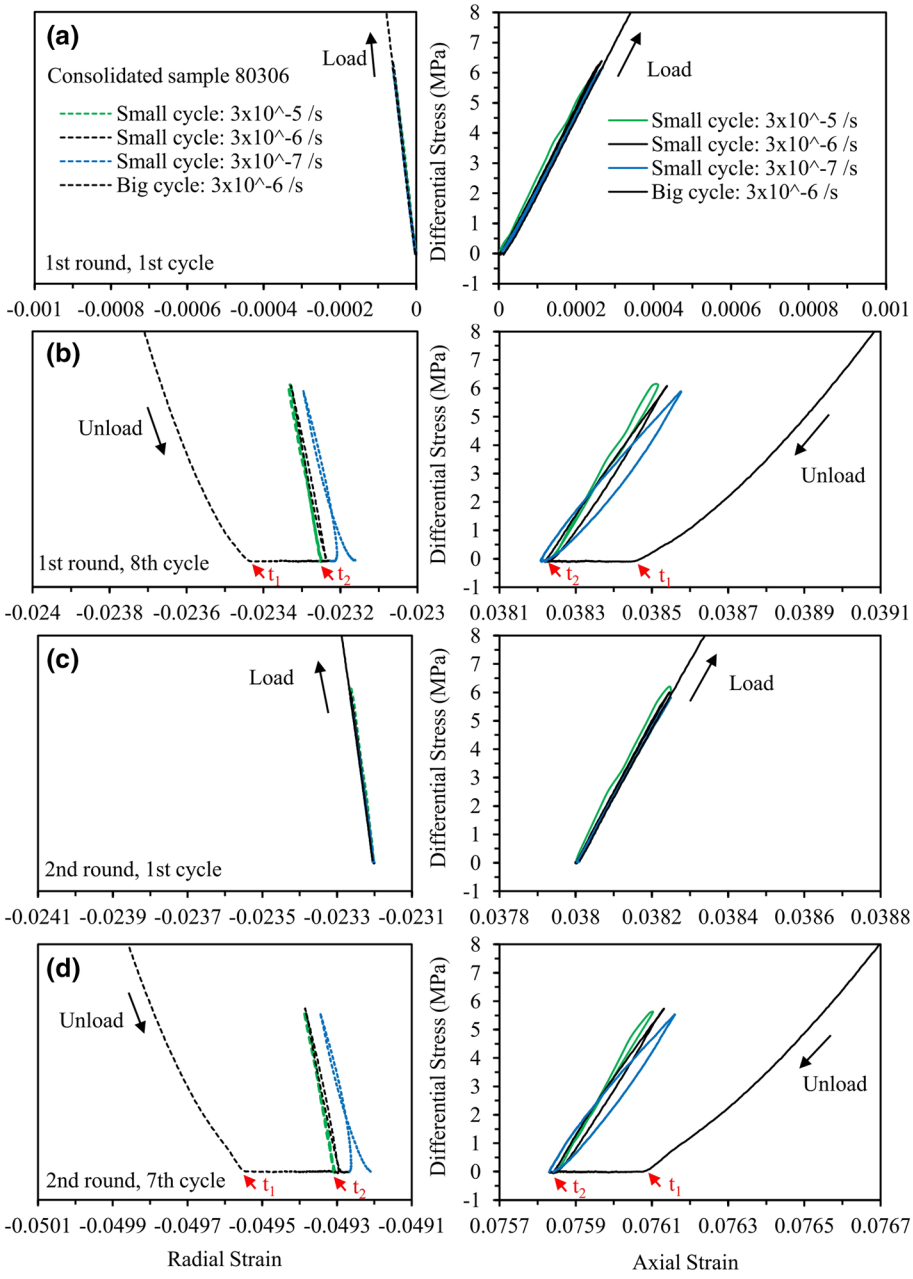

Figure 4. Plots of differential stress versus axial and radial strain of small-load cycles for consolidated sample 80306. The first (a and c) and last (b and d) small-load cycles for two rounds of cyclic compression tests are shown. Refer Figure 3a for locations of these small-load cycles in the overall stress-strain curve. Loading and unloading directions of large-load cycles are indicated by arrows. t_1 and t_2 mark the complete unload of a large cycle and the start of the first small cycle, respectively. Approximately 15 min was maintained between t_1 and t_2 to reduce the impact of time-dependent deformation from large-load cycles on subsequent small-load cycles.

second-round test, Young's modulus decreases quickly and develops pronounced rate-dependence, repeating the evolution shown in the first-round test. Overall, Poisson's ratio increases with increasing inelastic deformation (Figure 6b). Similar to the evolution of Young's modulus, Poisson's ratio is initially independent of strain rate, but progressively increases in rate-dependence with increasing inelastic deformation. After the hold, Poisson's ratio recovers significantly and returns to rate-independence, but then repeats the same evolution as seen in the prehold, first-round test.

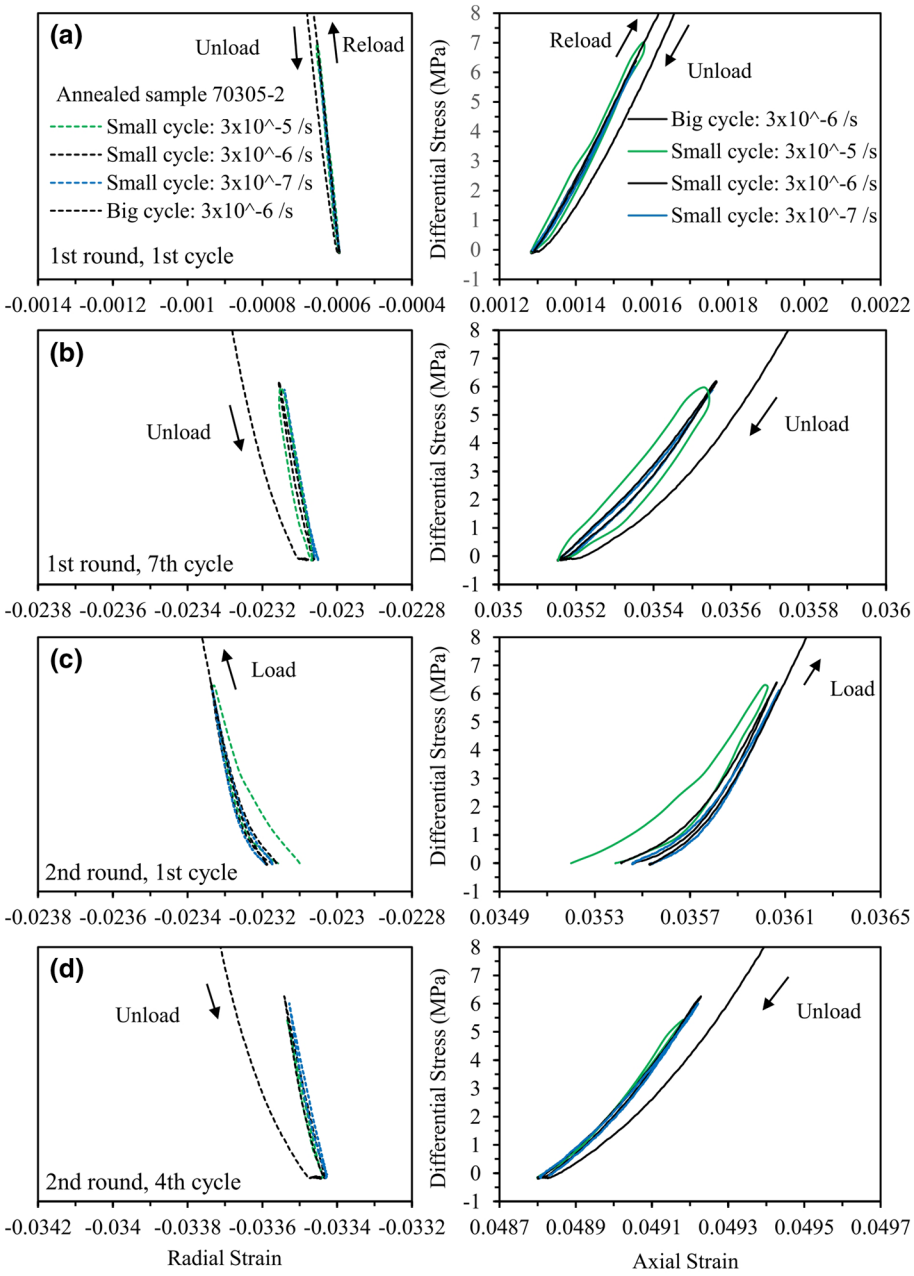

Figure 5. Plots of differential stress versus axial and radial strain of small-load cycles for annealed sample 70305-2. The first (a and c) and last (b and d) small-load cycles for two rounds of cyclic compression tests are shown. Refer Figure 3b for locations of these small-load cycles in the overall stress-strain curve. Loading and unloading directions of large-load cycles are indicated by arrows. Note in (b), the amplified hysteresis of the fastest small-cycle (shown in green) was caused by the loading procedure, likely a sticking of force gauge during rapid load/unload.

Young's modulus of annealed samples exhibits a different evolution with increasing inelastic deformation than that of consolidated samples (Figure 6c). In the first-round test of an annealed sample, Young's modulus is similar in the first two small-load cycles, but then decrease continuously thereafter. In the second-round test, after a hold for 66 h without confinement, the first small-load cycles show abnormally low Young's modulus due to closing of the unloading cracks (Figure 5c). In subsequent cycles, Young's modulus maintains similar values slightly lower than those of the last cycles of the first-round test, without any sign of recovery to the original values (i.e., at zero axial strain). Unlike the consolidated sample, Young's

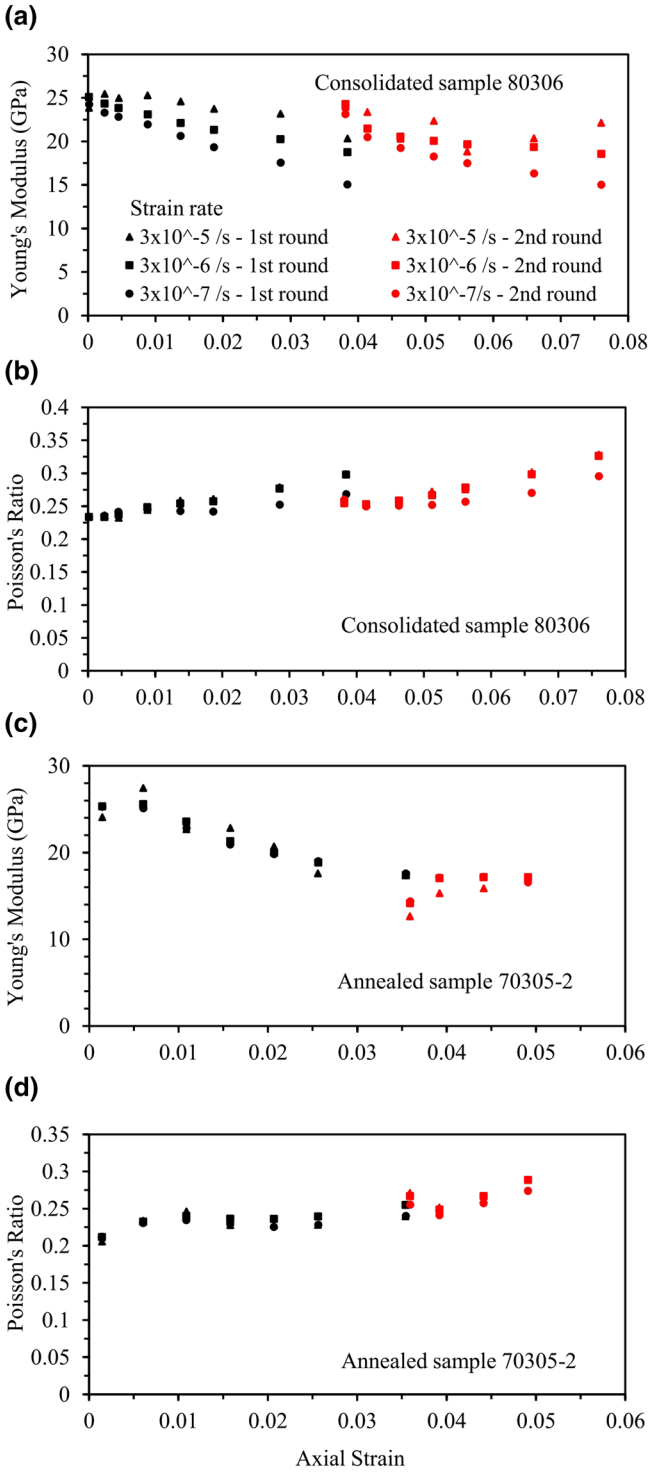

Figure 6. Plots of Young's modulus and Poisson's ratio as a function of axial strain for consolidated sample 80306 (a and b) and annealed sample 70305-2 (c and d). Young's modulus and Poisson's ratio were calculated for the loading segments of small-load stress cycles in the differential stress range between 2.5 and 5.5 MPa.

modulus of annealed samples is rate-independent regardless of the imposed inelastic strain. Poisson's ratio of annealed samples increases with increasing inelastic strain (Figure 6d). Neither strain rate nor a long hold affects the evolution of Poisson's ratio.

3.1.4. The Effects of Holds on Elastic Properties

As shown by the measurements of Young's modulus and Poisson's ratio, imposing a hold leads to a recovery from the reduced values produced during permanent flow to nearly original values (prior to the permanent deformation). The recovery occurs very rapidly in consolidated samples; experiments show the Young's modulus recovers to 96% of the original values in less than 22 h. The rapid recovery did not require confining pressure or differential stress.

Elastic properties of annealed samples do not recover after a hold at zero pressure for 66 h, but only because of the presence of the unloading cracks (Figure 5c); recovery of elastic properties does occur once unloading cracks are closed at 1 MPa confining pressure (Figure 7). Nonetheless, compared to consolidated samples, recovery in annealed samples is much slower even if the sample is under pressure and stress. After ~27 h under confining pressure, Young's modulus recovers to only 66%–71% of the original value. With additional ~90 h under both pressure and differential stress (during stress relaxation test), Young's modulus recovers to 89% of the original value.

3.1.5. Stress Relaxation Behavior

The stress relaxation tests were initiated at high differential stress after accumulating permanent strain by semibrittle flow during a large-load cycle. Qualitatively, the stress relaxation behavior of the consolidated and annealed samples is markedly different. The consolidated sample displays much greater relaxation of stress over a longer period of time before achieving a strain rate of 10^{-9} s^{-1}, whereas the annealed sample displays less relaxation of stress over a shorter period of time until the strain rate achieves 10^{-9} s^{-1} (Figure 8).

Stress relaxation data of axial strain rate versus differential stress plotted in logarithmic scale may be used to identify operation of different time-dependent microprocesses by comparing the slope of the relaxation curve (exponent of a power-law creep relation) between the different samples and within a single sample as a function of stress. The stress exponents have characteristic values for micromechanisms such as dislocation glide and diffusion, which are well documented for salt (Haupt, 1991; Spiers et al., 1986; Zhang et al., 2007). The slope of the stress relaxation curve for the consolidated samples decreases continuously with strain rate, but is linear below a strain rate of 2×10^{-8} s^{-1} with a stress exponent of 0.9 (Figure 8). A stress exponent of unity reflects linear viscous behavior which is consistent with diffusion creep. The stress relaxation behavior of annealed samples shows a relatively constant slope over the range of strain rate of 5×10^{-6} s^{-1} to 4×10^{-10} s^{-1} with an exponent ~25 (Figure 8). The observed exponent is consistent with deformation by dislocation glide in salt (Spiers et al., 1986; Zhang et al., 2007). The observed behavior is also consistent with stress relaxation by frictional sliding in salt.

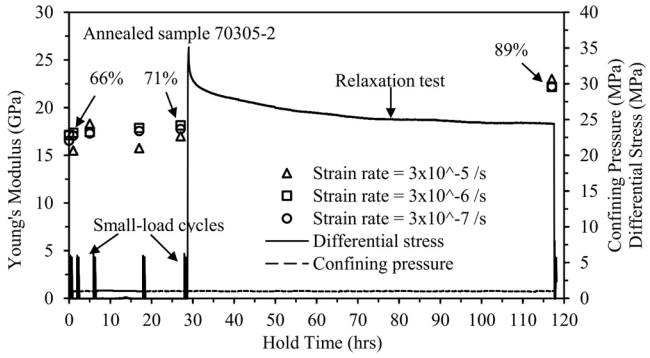

Figure 7. Plots of Young's modulus and differential stress as a function of hold time for annealed sample 70305-2. The hold time is relative to the end of the last (fourth) small-load cycles of the second-round test in Figure 3b. Percentage numbers are relative to the original Young's modulus (i.e., at zero axial strain).

3.2. Microstructures

3.2.1. Starting Material

An unconsolidated sample of granular salt consists of cubic-shaped grains with fairly sharp corners and show very little evidence of dislocation structures after etching (Figure 9a). Individual grains often contain fluid inclusions that appear as dark pits in the petrographic image. Fluid inclusions exhibit cubic, tubular or irregular shapes and may be isolated or arranged in linear arrays. Fluid inclusion size varies from tens of microns to less than one micron.

After consolidation, the initially cubic grains have more rounded corners and other indentations due to intracrystalline plastic deformation at loaded grain contacts (Figure 9b). Grain contacts appear fully closed and are often straight or only slightly curved recording mutual indentation. Pores (equant voids) are present at places where the boundaries of three or more grains come together. The dominant intragranular substructure are the well-developed, dense, arrays of linear etch features, termed slip lines. The wavy slip lines are indications of dislocation glide controlled by cross slip of screw dislocations (Senseny et al., 1992; Spiers & Carter, 1996). The slip lines within individual grains are generally similar in orientation reflecting crystallographic control. At indented grain contacts where deformation is most intense, intersecting sets of slip lines in two or more orientations are present and diminish in number away from the contact. Some of the most highly strained areas contain small recrystallized grains, characterized by straight boundaries and dislocation-feature-free interiors. The recrystallized grains are uncommon, occurring in less than 4.8% of all grains. The recrystallized grains formed at the expense of the highly deformed grains, and likely at the latest stages of consolidation or under static conditions after consolidation was terminated because the grain boundaries are straight and the interiors are largely devoid of slip lines. Isolated intragranular microcracks are formed during consolidation that typically intersect fluid inclusions or coincide with fluid inclusion arrays, likely reflecting stress concentration at inclusions that nucleate cracks. Less than 6.4% of all grains contain intragranular cracks, which indicates limited influence of fracture during consolidation. Overall, grain boundaries are well bonded with presence of dense and irregular-shaped fluid inclusions (Figure 10a and 10b); the grain-boundary fluid inclusions typically measure less than 10 μm in length.

For the annealed samples, which are produced by static recrystallization of consolidated samples, are wholly comprised of strain-free, irregular to crudely polygonal grains forming imperfect triple junctions with gently curved grain boundaries (Figure 9f). All grain contacts are fully closed and pores (e.g., voids at triple junctions) are not observed at the optical microscopic scale. No microcracks are observed in annealed samples. Grain boundaries are well bonded and display dense and nearly equal-dimension fluid inclusions that measure less than a few microns in diameter (Figure 10e and 10f). Annealing reduced the fluid inclusion density and removed most of the larger fluid inclusions in grain interiors consistent with the much lower water content than in the consolidated samples.

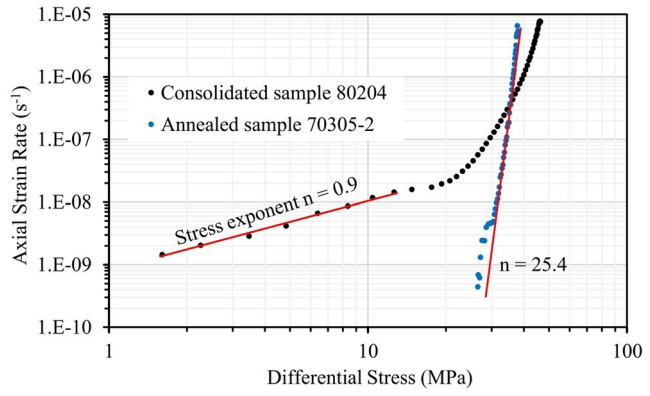

Figure 8. Plots of axial strain rate versus differential stress derived from stress relaxation tests for consolidated sample 80204 and annealed sample 70305-2. Stress exponents are determined for deformation regimes by linear fitting to data shown by the red lines.

3.2.2. Deformed Samples

Triaxial compression of consolidated samples led to an increase in the density of slip lines, characterized by an overall darker appearance in photomicrographs (compare Figure 9b with Figures 9c–9e). Two sets of recrystallized grains are observed, but the fractional area of recrystallized grains is low, ranging from 3% to 7%. One set of recrystallized grains appear undeformed and show no sign of dislocation substructure, whereas the other set are slightly deformed and display wavy slip lines with similar characteristics to grains in consolidated samples (Figure 9c). The majority of recrystallized grains appear in euhedral shapes and reside either

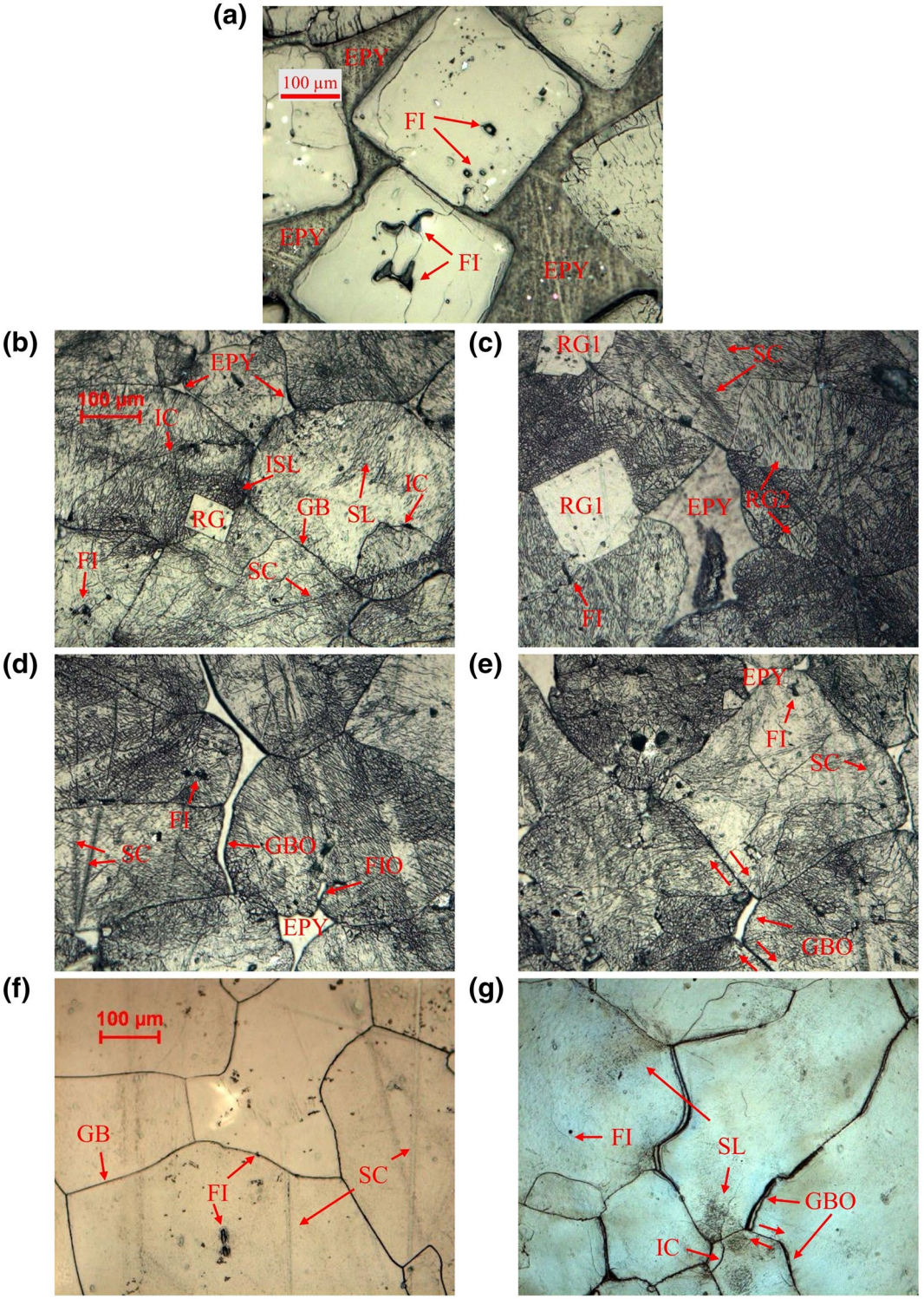
(a)
EPY
100 μm
FI
EPY
FI
EPY
(b)
EPY
100 μm
IC
ISL
IC
RG
GB
SL
FI
SC
(c)
RG1
SC
RG1
EPY
RG2
FI
(d)
FI
SC
GBO
FIO
EPY
(e)
EPY
FI
SC
GBO
(f)
100 μm
GB
FI
SC
(g)
FI
SL
GBO
IC

at grain boundaries or within highly deformed grains close to fluid inclusions. Grain shape analysis was performed on consolidated samples triaxially deformed to different axial strain to evaluate the role of grain flattening by intracrystalline plasticity. Grains were best fit by ellipses with the same area as the grain to determine the minor to major axis ratios. Consolidated samples triaxially deformed to 0%, 2.77%, and 7.31% axial strain are characterized by grain axial ratios of 0.671 ± 0.172 (131 grains), 0.650 ± 0.174 (215 grains), and 0.639 ± 0.162 (211 grains), respectively. The axial strain by grain flattening is estimated to account for around 6% of the total axial strain.

The most obvious deformation feature produced during the triaxial deformation of consolidated samples are grain-boundary opening-mode cracks (gbo cracks). An opening mode is easily identified if the grain boundary geometry on the two sides of the opening match exactly, suggesting they were previously in contact (Figure 9d and 9e). The gbo cracks distribute uniformly across samples and preferentially orient parallel or subparallel to differential load axis (Figure 11a). In many cases, two gbo cracks link by connecting to a common pore. The density, aperture, and linking of the gbo cracks increase with increasing inelastic strain and linked crack arrays comprised of several gbo cracks develop at large axial strain (Ding et al., 2017). Intragranular cracking is minor and often associated with fluid inclusions. Some of the fluid inclusions in grain interiors, shown as dark pits in micrographs, show greater opening than generally observed in consolidated samples, which records additional cracking caused by differential loading (Figure 11a). In the consolidated sample deformed to an axial strain of 7.31%, only 7.6% of all grains contain intragranular cracks, which is slightly higher than the background intragranular cracks density of 6.4% observed at zero axial strain. Of all the intragranular cracks, 81% are associated with fluid inclusions.

Under transmitted-light microscopy, high-density and irregular-shaped fluid inclusions are observed at closed grain boundaries of deformed samples (Figure 10c and 10d). The fluid inclusions appear in all closed grain boundaries. The morphology of the fluid inclusions is similar to that of the consolidated samples prior to triaxial deformation (compare Figure 10b with Figure 10d).

Triaxial deformation of the annealed samples produced wavy slip lines in the initially strain-free halite grains (Figure 9f). The slip lines are mostly concentrated near grain contacts reflecting indentation. The density of slip lines is much lower than that generally observed both before and after triaxial deformation of consolidated samples. Newly recrystallized grains are not observed in the annealed samples after triaxial deformation. Grain shape analysis shows similar minor-to-major axial ratio for an undeformed sample (0.652 ± 0.154, 166 grains) and a sample triaxially deformed to 4.87% axial strain (0.652 ± 0.165, 104 grains). The similar grain axial ratios suggest that grain flattening during triaxial deformation of the annealed sample is insignificant.

Grain-boundary opening cracks are present in the triaxially deformed annealed samples (Figure 11b). Two sets of gbo cracks are identified. One set of gbo cracks are oriented at low angle to load axis and occur as either isolated cracks along a single boundary between two grains, or a series of cracks linked in the direction of the differential load. This set of cracks are formed during triaxial deformation and are similar to the gbo cracks linked at pores in the deformed consolidated samples. The other set of gbo cracks in the deformed annealed samples are unloading cracks in various orientations but that are linked in the direction perpendicular to the differential load axis. The second set were produced during depressurization of the sample at

Figure 9. Reflected-light photomicrographs of (a) the starting microstructure of reagent-grade granular salt, sample 60209R, (b) a consolidated sample, 70516, prior to triaxial deformation, (c) a consolidated sample, 61003, triaxially deformed to 2.77% axial strain, (d and e) a consolidated sample, 61123, triaxially deformed to 7.31% axial strain, (f) an annealed sample, 61030, prior to triaxial deformation, and (g) an annealed sample, 070304, triaxially deformed to 4.87% axial strain. In all cases, the polished surfaces were chemically etched to illuminate microstructures. GB—grain boundary, GBO—grain boundary opening, EPY—epoxy (filling larger pores), RG—recrystallized grain, SL—slip lines, ISL—intersected slip lines, FI—fluid inclusions intersected by the polished surface, FIO—fluid inclusion opening, IC—intragranular cracks, SC—scratch associated with polishing. Paired arrows show inferred shear motion on grain boundaries associated with grain-boundary opening. For the photos of the triaxial deformed samples, differential load axis is vertical. Scale for (b–e) is shown in (b); scale for (f and g) is shown in (f). Note two types of recrystallized euhedral grains are shown in (c): RG1—recrystallized grains free of dislocation, RG2—recrystallized grains containing slip lines.

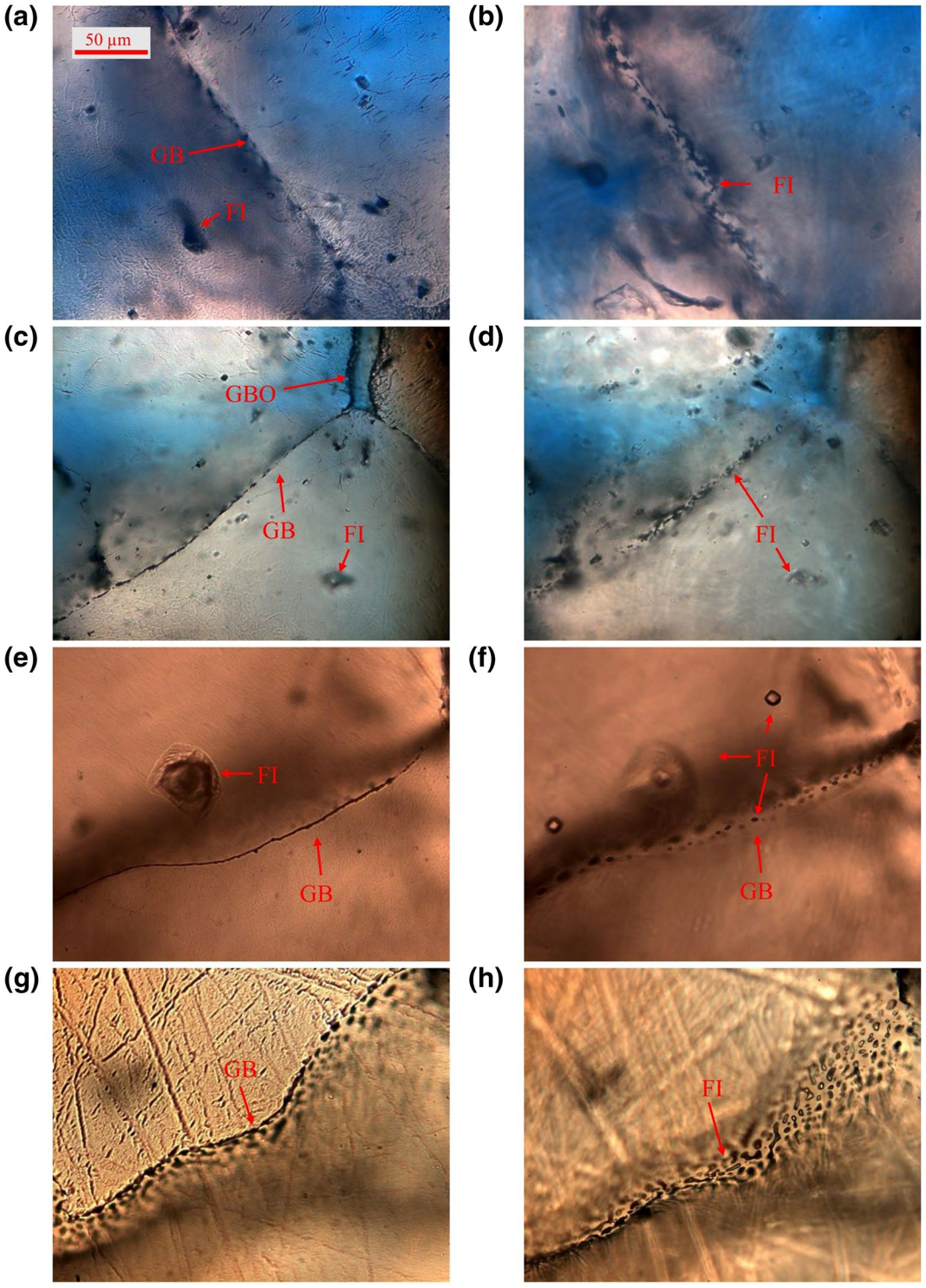

Figure 10. Transmitted-light photomicrographs of (a and b) consolidated sample, 70516, prior to triaxial deformation, (c and d) consolidated sample, 61123, triaxially deformed to 7.31% axial strain, (e and f) annealed sample, 61030, prior to triaxial deformation, (g and h) annealed sample, 70304, triaxially deformed to 4.87% axial strain. (a, c, e, g) The optical focus is on the polished surface; (b, d, f, h) The optical focus is below the polished surfaces to reveal grain boundary structures. For all cases the polished surface was chemically etched. GB—grain boundary, GBO—grain boundary opening, FI—fluid inclusions intersecting the polished surface. Differential load axis was vertical. Scale is shown in (a). Note fluid inclusions are observed along all grain boundaries.

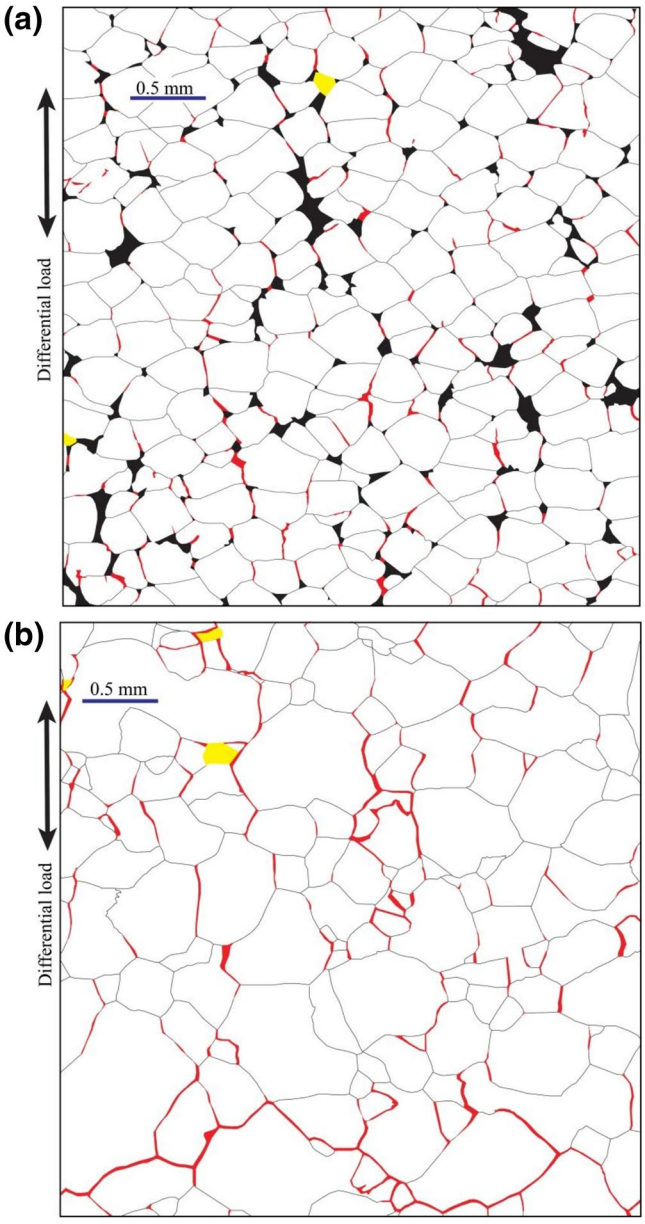

Figure 11. Tracings of stitched photomicrographs of (a) a consolidated sample, 61123, triaxially deformed to 7.31% axial strain, and (b) an annealed sample, 70304, triaxially deformed to 4.87% axial strain. Halite grains (white), pores (black), and opening-mode microcracks (red) were manually traced. Missing grains (yellow) resulted from plucking during polishing. Images were taken of the center of the sample. Note two sets of grain boundary openings in (b): one set preferentially aligned to the load axis (vertical direction) and distributed across the micrograph; the other set connected in the direction perpendicular to load axis (horizontal direction) and localized at the bottom of the micrograph, which are interpreted as unloading cracks formed during final depressurization.

the end of the triaxial deformation experiment and unrelated to the semibrittle flow during the large load-cycles. Intragranular cracking is also minor in triaxially deformed annealed samples. In the sample deformed to 4.87% axial strain, 7.7% of total grains contain intragranular cracks.

Viewed under transmitted-light optical microscopy, high-density and spherical or tubular-shaped fluid inclusions are apparent at the closed grain boundaries of the triaxially deformed annealed samples (Figure 10g and 10h). The fluid inclusions appear in all closed grain boundaries. Comparing with the undeformed annealed samples, grain-boundary fluid inclusions in the triaxially deformed annealed samples are less equant with more tubular shapes (compare Figure 10f with Figure 10h).

4. Discussion

4.1. Deformation Mechanisms

In consolidated samples, intracrystalline plasticity is an active deformation mechanism during the cyclic triaxial compression tests. First, the density of wavy slip lines after triaxial deformation is increased beyond that seen in the grains deformed by consolidation only. Second, wavy slip lines are observed in the recrystallized grains formed at the end of consolidation, but are absent from the recrystallized grains formed at the end of triaxial deformation, also demonstrating dislocation motion during triaxial deformation. At room temperature, low confining pressure, and relatively fast strain rates, dislocation glide is the dominant intracrystalline plastic process in halite as recovery mechanisms are insufficient (Carter & Hansen, 1983; Peach & Spiers, 1996; Senseny et al., 1992). However, two lines of evidence indicate dislocation glide is a subordinate mechanism. During triaxial deformation, the stress-strain behavior is flow at a nearly constant differential stress after yield, contrasting with a characteristic behavior of strain hardening during deformation by dislocation glide in polycrystalline halite at room temperature and higher pressure (Peach & Spiers, 1996). In addition, grain flattening is relatively insignificant in that it contributes only around 6% to the total axial strain.

The dominant micromechanism contributing to strain during triaxial deformation of the consolidated samples is cracking, opening, and sliding along grain boundaries that allows grain rearrangement (Shen, Ding, Lordkipanidze, et al., 2021). The gbo cracking occurs at all stages of axial shortening and is recorded by increase in crack density and aperture with increased axial strain (Figure 11a). Moreover, opening cracks produce new porosity that explains the observed dilatancy throughout triaxial deformation (Figure 3a). Based on the geometry and distribution of gbo cracks, shear motion can be confidently inferred along adjacent closed grain boundaries (Figure 9e). Here, we refer to the shear motion along grain boundaries with the descriptive term, grain-boundary sliding (gbs), that is, the mechanism of sliding is not implied.

The observational evidence of the dominant and subordinate micromechanisms operative during triaxial deformation of consolidated samples suggest that the grain boundaries are weak surfaces relative to grain interiors when oriented at low to moderate angles to the differential load axis. During initial sample fabrication by uniaxial consolidation of granular halite, the lateral stress is raised with axial stress and gbo is greatly inhibited. Thus grain rearrangement and pore volume reduction is achieved by gbs and indentation via dis-

location glide, such that grain interiors are hardened (Shen, Ding, Lordkipanidze, et al., 2021). Subsequent triaxial deformation at low temperature and confining pressure promotes brittle processes along relatively weak grain boundaries. Thus, bonding along optimally oriented grain boundaries is progressively damaged by increasing gbo and gbs. Halite grains with broken boundaries rearrange through gbs and gbo, but due to sufficient confining pressure the gbs cannot be accommodated completely by gbo without some concomitant intragranular deformation by dislocation glide.

Cracking, opening, and sliding along grain boundaries also is important during the cyclic triaxial compression tests on annealed samples (Figure 11b), most clearly evinced by the increase in sample volume (Figure 3b) and gbo crack-arrays. While grain-scale plastic deformation by dislocation glide may have contributed to gbo, there is clear kinematic evidence that gbs contributed to opening (Figure 9g) as occurred in the consolidated samples. Thus, optimally oriented grain boundaries are weak relative to the grain interiors of annealed samples at the test conditions. Intracrystalline plasticity is significantly more important for deformation of the annealed samples during the cyclic triaxial compression test compared to the microprocesses of deformation in the consolidated samples. Static recovery and recrystallization during annealing reduce dislocation density to produce strain-free grains and reduced critical shear stress for dislocation glide (Figure 9f). The triaxial deformation leads to dislocation motion evidenced by the formation of wavy slip lines (Figure 9g). While consolidated samples flow at nearly constant stress, the annealed samples yield at much lower differential stress and show pronounced work hardening in the stress-strain response (Figure 3), consistent with significant deformation by intracrystalline dislocation glide. The lack of evidence for grain flattening in the annealed samples likely reflects the lack of initial porosity that accommodates grain flattening by indentation as occurred in the consolidated samples with a porous-granular structure. Overall, for the annealed samples, dislocation glide contributes significantly to the deformation of the annealed samples, but also is likely a subordinate deformation mechanism relative to the gbo cracking and gbs at the test conditions.

Grain-boundary cracking and intracrystalline plasticity also are documented by Peach and Spiers (1996) and Bourcier et al. (2013) in synthetic, annealed, salt-rock samples, and deformation conditions similar to annealed samples herein. While Peach and Spiers (1996) focused on the effect of microcracking in transport properties of salt-rock, Bourcier et al. (2013) quantified strain partitioning between gbs and intracrystalline plasticity using surface markers and digital image correlation. These works conclude that gbs accounts for more than 50% of total strain in fine-grained (0.03–0.08 mm) samples, and intracrystalline plasticity accounts for more than 80% in coarse-grained (0.25–0.5 mm) samples. Given that our annealed samples have a greater range of grain size (0.025–0.833 mm), and were deformed to a greater total strain (~8% relative to ~3%), our interpretation of dominant and subordinate deformation mechanisms is in good agreement with previous findings. For both consolidated and annealed samples, the stress states during semibrittle flow fall in the dilatancy field mapped out by previous works on salt-rocks (Alkan et al., 2007; Hunsche & Hampel, 1999; Popp & Kern, 2000; Popp et al., 2001). The dilatancy field is characterized by increased pore volume caused by microcracking, which is consistent with mechanical and microstructural observations from our deformed samples. For both types of triaxially deformed samples, grain boundaries can be classified into two groups based on whether they open under differential load (Figure 12). Grain boundaries that open and create new porosity are preferentially aligned to load axis. Grain boundaries that remain closed can be further divided into two subgroups based on whether sliding occurs. Those oriented at low to moderate angles to load axis are subjected to sufficient shear stress to cause sliding during differential loading, while those oriented at high angles generally are not.

4.2. Micromechanisms of Grain Boundary Sliding

In the brittle field, slip along grain boundaries displays frictional behavior (pressure dependence of shear strength) arising from microfracture and local separation along nonplanar surfaces such that the true area of contact is less than the apparent area (Bowden & Tabor, 2001; Scholz, 2019). Locally, associated with indentation creep at contacting asperities, intracrystalline processes such as dislocation glide also may occur (Dieterich, 1978). At room temperature, low confinement, and high strain rates, shear

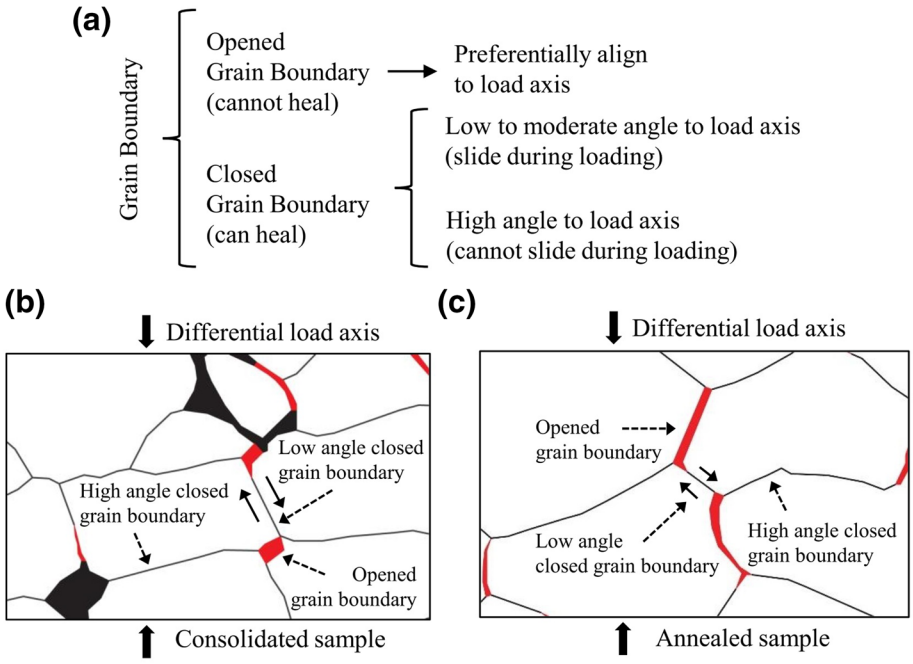

Figure 12. Classification of grain boundaries in deformed samples: (a) classification chart and microstructural examples of (b) consolidated and (c) annealed samples. In (b and c), halite grains (white), pores (black), and opening-mode microcracks (red) were manually traced. Paired arrows show inferred shear motion at a closed grain boundary.

of granular salt displays frictional behavior with microstructural evidence of fracture, grain crushing, and intracrystalline plasticity, and macroscopic coefficient of friction, μ, between 0.5 and 1 (Chester & Logan, 1990; Shimamoto, 1986). These studies demonstrate an increase in the role of intracrystalline plasticity and concomitant reduction in pressure dependence of strength within the semibrittle field at higher pressure and temperature or decreased strain rate (Chester, 1988a; Shimamoto, 1986). Accordingly, in the present triaxial experiments at low confining pressure, room temperature and moderate strain rate, the observed gbs is likely frictional. For semibrittle flow of the consolidated samples, the differential stress of 40 MPa and confining pressure of 1 MPa produces shear and normal stress on grain boundaries at angles 45° to the sample axis, which is sufficient for frictional slip with a coefficient of friction of 0.95, assuming stress homogeneity. Grain boundaries deemed likely to have slipped in the deformed samples, based on linkage to pores or neighboring gbo cracks, have an average orientation of 50.4° and 53.4° to the sample axis in the consolidated and annealed samples, respectively. For these and greater angles, frictional sliding on grain boundaries is compatible with the range of friction coefficients observed in shear experiments on granular salt, particularly considering the likelihood of significant stress variation at the grain scale.

Frictional sliding generally is characterized by small magnitude rate dependence (Dieterich, 1978; Marone, 1998). Although the macroscopic semibrittle flow strength in stress cycling experiments was determined at a single strain rate, stress-relaxation tests can provide information on rate dependence of strength and the underlying mechanisms of sliding. The rate dependence of strength is clearly different for consolidated and annealed samples as shown by the stress relaxation tests (Figure 8). The water content of the annealed samples is 5.1 ppm prior to triaxial deformation. This water content is comparable with the "dry samples" of Watanabe and Peach (2002), which deformed without the operation of fluid-assisted grain-boundary processes (Bos & Spiers, 2002a; Pennock et al., 2006). Thus, gbs accommodated by fluid-assisted diffusion is likely negligible in the annealed sample. The small rate dependence shown by the stress relaxation behavior at strain rates down to 10^{-10} s^{-1} ($d\mu/d\ln\ \dot{\epsilon} \cong 0.002$) is comparable to the observed rate dependence of frictional sliding in salt and other rocks (Chester, 1988a; Chester & Logan, 1990; Marone, 1998), as well as with the underlying process of indentation creep of asperity contacts by dislocation glide.

The consolidated samples are considered wet, with a water content of 301 ppm. For fine-grained salt-rocks (0.08–2 mm), this water content is sufficient to invoke fluid-assisted grain boundary processes such as grain-boundary migration recrystallization and solution-transfer creep as long as the water is located at the grain boundaries (Shen & Arson, 2019a; Spiers & Carter, 1996; Ter Heege et al., 2005; Watanabe & Peach, 2002). We infer that at low strain rates, gbs may be accommodated by water-assisted diffusion if water is distributed along the sliding grain boundaries. The diffusion process is likely localized and serves as an effective accommodation mechanism for gbs (Bos & Spiers, 2002a; Pennock et al., 2006; Raj & Ashby, 1971) and is compatible with the stress relaxation behavior at low strain rates with a stress exponent of nearly one (Figure 8). At higher strain rates in the consolidated samples, where flow strength is somewhat greater than that for the annealed samples, frictional sliding likely occurs in conjunction with water-assisted diffusion. In this latter case, the stress relaxation behavior from an initially high stress exponent evolving to a very low exponent (Figure 8) would be consistent with frictional gbs dominating at the beginning of relaxation (i.e., at high stress) and a gradual transition to diffusion gbs as the lowest rates (10^{-10} s^{-1}) are approached.

4.3. Elastic Properties and Associated Grain Boundary Behavior

The progressive changes in the elastic behavior for both consolidated and annealed samples during progressive deformation, as displayed in the small-load cycles, must be caused by the increase in porosity and change in pore distribution (in consolidated samples), and the significant role of gbs relative to pore and gbo cracks. For both sample types, Young's modulus and Poisson's ratio decreases and increases, respectively, with increasing inelastic deformation by semibrittle flow. The starting porosity of the consolidated samples, in the form of pores, produces little difference in elastic properties compared to the annealed samples in initial loading (Figure 6). The increase in porosity with progressive strain in both types of samples is similar, as is the generation of axial gbo cracks and linked gbs cracks, which explains the similar evolution of Young's modulus and Poisson's ratio. Semibrittle flow in the large-load cycles activates gbo cracking and frictional gbs. During small stress cycles, the gbo cracks can increase or decrease in aperture with associated gbs in a recoverable fashion. The increase in the density of gbo and gbs arrays with increasing strain, as evinced by the progressive increase in volume (Figure 3), leads to the observed continuous reduction in modulus and increase in Poisson's ratio with axial strain (Shen, Ding, Arson, et al., 2021).

The documentation that the changes in elastic properties during semibrittle flow in the consolidated sample are largely recovered after sufficiently long holds at confinement of 1 MPa or less, but not in the annealed sample, suggests water-assisted healing of the gbs cracks. The water-assisted diffusion processes responsible for the enhanced stress relaxation of the consolidated samples at low rates, also promote healing of gbs interfaces under isostatic stress conditions. Similar to the stress relaxation results, the lower water content in the annealed samples either prohibits or sufficiently slows down water-assisted diffusion such that healing does not occur in periods of tens of hours. Comparing microstructural observations before and after holds, no appreciable microstructural change was observed in the grain interior such as the density and distribution of slip lines, or closure of intragranular cracks and pores. However, microstructural observation of grain boundaries that had slid (evinced by linkage to gbo cracks) shows dense arrays of small fluid inclusions characteristic of crack-healing (Figure 10d and 10h; Roedder, 1984). Opened grain boundaries remain open and do not show evidence of rebonding (Figure 9d and 9e). Healed boundaries are restrengthened, so after a hold they would not slip during small stress cycling until additional semibrittle flow reestablishes gbs and redistribution of water.

After semibrittle flow of consolidated samples, during which water is distributed on the frictional gbs interfaces, rate-dependent elastic behavior is observed during subsequent small stress cycling. Cycling at lower strain rate leads to lowered modulus and greater hysteresis. The rate-dependence increases with axial strain, but is greatly reduced or disappears upon healing (Figure 6a and 6b). These observations can be understood by the fluid-assisted diffusional processes in sliding grain boundaries. In the small-load cycles, more pronounced diffusion at low strain rates leads to greater viscoelastic behavior. In a stress-strain plot, this is expressed as lower stiffness (more axial strain is recovered) and higher hysteresis (more work is done) (Figures 4b and 4d). Increasing semibrittle flow at large-load cycles activates more sliding grain boundaries,

which in turn leads to more pronounced hysteresis, rate-dependence, and anelasticity in small-load cycles (Shen, Ding, Arson, et al., 2021). These phenomena are absent in annealed samples due to insufficient water at grain boundaries.

4.4. Coupled Micromechanisms

Both the consolidated and annealed samples deform in the semibrittle flow field with a combined operation of intracrystalline-plastic mechanisms, intragranular cracking, gbo cracking, and by frictional gbs at the higher strain rates, and fluid-assisted diffusional gbs at the lower strain rates in the wet consolidated samples only. While intragranular cracking is subordinate, the displacement along linked arrays of gbs and gbo cracks formed at variably oriented grain-boundaries is the dominant microprocess for grain rearrangement and axial shortening. The gbs shear surface inclined to the load axis and neighboring gbo segments are analogous to the well-known shear and wing crack for failure of brittle materials (Erdogan & Sih, 1963; Griffith, 1924). For brittle elastic material, the shear displacement on the surface inclined to the loading direction is coupled with the opening and extension of the wing cracks, leading to an elastoplastic behavior. By analogy, for the case of salt-rock at semibrittle flow conditions, frictional gbs is coupled with gbo to produce pressure-dependent plastic behavior. However, for the case of the wet consolidated samples where gbs is by water-assisted diffusion processes, the coupling of gbs by diffusion and gbo by cracking lead to viscoplastic behavior during semibrittle flow at low strain rates, as well as viscoelastic behavior during small stress cycling represented by anelasticity and hysteresis (see also Shen, Ding, Arson, et al., 2021).

For semibrittle flow of the consolidated sample to axial strains of ~8%, significant intracrystalline plasticty occurs as evinced by grain flattening and mutual indentation at high-angle closed grain boundaries. Detailed fabric analysis of the consolidated samples deformed in triaxial compression to several sequential strains show that coordination of grains in the axial direction increases whereas coordination and solidity in the lateral direction decreases with strain (Shen, Ding, Lordkipanidze, et al., 2021). These changes reflect the rearrangement of grains into columns with high-angle closed grain boundaries, and with the concurrent formation of bounding crack networks gbo cracks aligned in the axial direction and gbs surfaces preferentially in the lateral direction (Shen et al., 2020). The microstructures and fabric evolution document the coupled operation of intracrystalline dislocation glide associated with shortening the columns of coordinated grains and as gbs and gbo with lateral grain motions for rearrangement. Thus, dislocation glide is a subordinate but necessary intragranular deformation mechanism for gbs and gbo to operate at the test conditions of pressure, temperature and strain rate.

In annealed samples, coupling of intracrystalline plastic and gbo and gbs processes during semibrittle flow is similar to that in the consolidated samples. The crack arrays are qualitatively similar to those in the consolidated samples, but because the annealed samples start with strain-free grains, the location of intracrystalline strain is identifiable by density of slip lines (Figures 9f and 9g). The locations of grains where increased slip line density occur during semibrittle flow coincide with regions of grain impingement resulting from incompatibility of grain rearrangements by motion along gbo and gbs arrays (Figure 9g). With increasing inelastic strain, the slope of the stress-strain curve decreases while the slope of volumetric strain-axial strain curve increases (Figure 3b), which indicates that the hardening rate decreases while dilatancy rate increases. In the early stage of deformation, grain-scale plastic deformation by dislocation glide in strain-free grains easily accommodates displacement incompatibilities associated with gbo and gbs to achieve the bulk triaxial deformation. With increasing dislocation density, continued glide requires higher stress for gbs and gbo to operate. In some ways, the consolidated sample may be viewed as representative of the final state of an annealed sample deformed at rates and temperatures where recovery processes are relatively slow and unimportant. These relations show that the intracrystalline plasticity is coupled with the gbo and gbs on linked crack arrays. As such, the gbo contributes pressure dependence and the intracrystalline plasticity contributes strain rate and temperature dependence, and strain hardening, to the bulk behavior. The microprocesses operating together in the consolidated and annealed samples during semibrittle deformation constitute a distinct flow process reflecting series-sequential operation of the micromechanisms rather than independent, parallel-concurrent micromechanisms.

4.5. Implications

Our experiments document coupled brittle frictional, crystal-plastic, and diffusional microprocesses during semibrittle flow that operate as series-sequential. Under this mode of deformation, the flow strength likely exhibits pressure dependence associated with the microcracking and friction, and rate and temperature dependence with intracrystalline plasticity and diffusion. Such a coupled deformation process should be represented as a distinct mechanism field in deformation-mechanism maps (e.g., Chester, 1988a). Similarly, the brittle-plastic transition in the strength profiles of the crust and lithosphere should also be represented as a distinct transition zone that is likely much different than represented by assuming independent mechanisms (e.g., Shimamoto, 1989).

The coupled microprocesses lead to distinct rheologic behavior that could have implications for earthquake mechanics in the brittle-plastic transition zone. Our experiments document significant transient behaviors associated with stress cycling, which can be explained by path-dependent activation of water-assisted diffusion processes and termination by static healing. Numerical modeling of our experimental data also demonstrates the association of transient semibrittle behavior with stress cycling (Shen, Ding, Arson, et al., 2021). In the lithosphere, the brittle-plastic transition is characterized by semibrittle deformation involving brittle frictional, crystal-plastic, and diffusional processes (Brace & Kohlstedt, 1980; Kirby, 1980; Kohlstedt et al., 1995). In seismogenic zones of the crust, the brittle-plastic transition corresponds to the depth limit of shallow crustal seismicity and experiences pronounced stress cycling (Brace & Kohlstedt, 1980; Sibson, 1983). In deep crust, there are also evidences of elevated pore pressure which is thought to enhance brittle deformation despite high stress and temperature conditions (Beeler et al., 2016). During interseismic periods, the upper part of brittle-plastic transition deforms dominantly by brittle friction and accumulate stress, whereas the lower part deforms viscously near steady state (Scholz, 2019; Sibson, 1983, 1986). Viewing salt as rock analog material, the consolidated samples may represent the shallower, brittle-frictional end-member of the semibrittle regime, and the annealed samples may represent the deeper, viscous-plastic end-member. Earthquakes rupture downward into the semibrittle zone, effectively creating large displacement and concentrated increase in stress and strain rates (Strehlau, 1986), which may be qualitatively analogous to the large-load cycles employed in this study. The pronounced stress cycling by earthquakes may cause the healed or recrystallized rocks to yield and undergo semibrittle flow, activating grain boundaries and redistributing water. Postseismic deformation may involve time-dependent grain-boundary sliding that effectively relax stress. As stress is reduced, rocks may eventually heal at grain boundaries at shallow depths or transition back to steady state creep with recrystallization before next stress cycle. Consequently, profound transient perturbation in the lithosphere could activate completely different deformation microprocesses that alter rock rheological behavior during seismic cycles. Certainly, this is a rather simplified analogy to natural rock deformation by ignoring many factors such as rock composition and heterogeneity. However, it serves to illustrate the important role of grain-boundary processes in controlling rheological behavior of rock at semibrittle conditions.

In salt caverns, similar conditions of low temperature and effective pressure that promote semibrittle deformation in our experiments may be encountered at cavern walls (Bérest, 2013; Brouard et al., 2012; Wang et al., 2018). In excavated salt caverns, halite grains at walls increase in dislocation density due to construction related deformation, whereas in solution mined caverns dislocation density in halite grains at walls should be as low as in nondisturbed natural salt (Fokker, 1995). In gas storage caverns operated to satisfy the seasonal or emergency needs, the cyclic loading associated with changes in gas volume will induce stress cycling (Bérest, 2013) analogous to our experiments. Inelastic deformation from large stress cycles around salt cavern walls could lead to the development of grain boundary cracking and frictional sliding to redistribute water, which can activate viscous processes. Linking of preferentially opened grain boundaries with shear slipping boundaries can produce linked arrays that, with further stress cycling, could cause instability of cavern wall such as spalling and block fall (Ding et al., 2017). Avoidance of large stress cycling could minimize breakage and activation of frictional sliding with dilatancy from associated opening boundaries, and employing holds to allow stress relaxation and healing of cracked grain boundary could help preserve the integrity of cavern walls. Additionally, as water is almost always present in natural salt rocks (Roedder, 1984), elastic deformation may be dependent on loading rate with pronounced hysteresis at low strain rates in between stress cycles. Numerical mod-

eling of salt caverns should consider the time-dependent behavior of salt and the consequent damage and healing processes, which will affect the mechanical behavior and sealing capability of salt caverns (Arson, 2020; Shen & Arson, 2019b).

5. Conclusions

We conducted cyclic triaxial compression and stress relaxation tests on two types of synthetic salt-rocks with contrasting grain structures at room temperature and low confinement. Mechanical behavior and microstructures document semibrittle deformation in both samples involving grain-boundary opening and sliding, dislocation glide, intragranular cracking. These brittle and viscous mechanisms are coupled as series-sequential to achieve flow. Large stress cycling activates grain-boundary sliding accommodated by frictional processes at high strain rates and/or dry condition, or by pronounced fluid-assisted diffusion at low strain rates and presence of fluid. Young's modulus and Poisson's ratio are largely controlled by the microprocesses at linked open and closed grain boundaries, leading to viscoelastic and hysteretic behaviors. Such time-dependent effects vanish with grain-boundary healing over days-long holds at low differential stress. The coupling of micromechanisms suggests that semibrittle deformation is more appropriately represented as a distinct rheologic zone in both deformation-mechanism maps and lithosphere strength profiles. The observed semibrittle processes in response to stress and strain rate cycling in experiments suggest that in the lithosphere, stress and strain rate changes associated with the earthquake cycle would produce variation in semibrittle microprocesses and mechanical behavior with time as well as with depth.

Data Availability Statement

The data used in this study are available at the Texas Data Repository (https://doi.org/10.18738/T8/QCHJEM).

Acknowledgments
The authors are grateful to Chris Spiers, Colin Peach, Peter van Krieken, and others at Utrecht University for guidance in salt microscopy techniques. Special thanks go to Andreas Kronenberg for assistance in measuring water content and numerous discussions. We would also like to thank Janos Urai, an anonymous reviewer, the Associate Editor, and Editor for their helpful comments. Financial support for this research was provided by the National Science Foundation, Awards CMMI-1361996 (TAMU) and CMMI-1362004 (GT).

References

Alkan, H., Cinar, Y., & Pusch, G. (2007). Rock salt dilatancy boundary from combined acoustic emission and triaxial compression tests. *International Journal of Rock Mechanics and Mining Sciences*, *44*(1), 108–119. https://doi.org/10.1016/j.ijrmms.2006.05.003

Arson, C. (2020). Micro-macro mechanics of damage and healing in rocks. *Open Geomechanics*, *2*, 1–41. https://doi.org/10.5802/ogeo.4

Beeler, N. M., Hirth, G., Thomas, A., & Bürgmann, R. (2016). Effective stress, friction, and deep crustal faulting. *Journal of Geophysical Research: Solid Earth*, *121*, 1040–1059. https://doi.org/10.1002/2015JB012115

Bérest, P. (2013). *The mechanical behavior of salt and salt caverns*. Paper presented at ISRM International Symposium—EUROCK 2013, International Society for Rock Mechanics and Rock Engineering, Wroclaw, Poland.

Bos, B., Peach, C. J., & Spiers, C. J. (2000a). Frictional-viscous flow of simulated fault gouge caused by the combined effects of phyllosilicates and pressure solution. *Tectonophysics*, *327*(3), 173–194. https://doi.org/10.1016/S0040-1951(00)00168-2

Bos, B., Peach, C. J., & Spiers, C. J. (2000b). Slip behavior of simulated gouge-bearing faults under conditions favoring pressure solution. *Journal of Geophysical Research*, *105*, 16699–16717. https://doi.org/10.1029/2000JB900089

Bos, B., & Spiers, C. J. (2001). Experimental investigation into the microstructural and mechanical evolution of phyllosilicate-bearing fault rock under conditions favouring pressure solution. *Journal of Structural Geology*, *23*(8), 1187–1202. https://doi.org/10.1016/S0191-8141(00)00184-X

Bos, B., & Spiers, C. J. (2002a). Fluid-assisted healing processes in gouge-bearing faults: Insights from experiments on a rock analogue system. *Pure and Applied Geophysics*, *159*, 2537–2566. https://doi.org/10.1007/s00024-002-8747-2

Bos, B., & Spiers, C. J. (2002b). Frictional-viscous flow of phyllosilicate-bearing fault rock: Microphysical model and implications for crustal strength profiles. *Journal of Geophysical Research: Solid Earth*, *107*(B2), ECV1-1–ECV1-13. https://doi.org/10.1029/2001JB000301

Bourcier, M., Bornert, M., Dimanov, A., Héripré, E., & Raphanel, J. L. (2013). Multiscale experimental investigation of crystal plasticity and grain boundary sliding in synthetic halite using digital image correlation. *Journal of Geophysical Research: Solid Earth*, *118*, 511–526. https://doi.org/10.1002/jgrb.50065

Bowden, F. P., & Tabor, D. (2001). *The friction and lubrication of solids*. Oxford, England: Oxford University Press.

Brace, W. F., & Kohlstedt, D. L. (1980). Limits on lithospheric stress imposed by laboratory experiments. *Journal of Geophysical Research*, *85*, 6248–6252. https://doi.org/10.1029/JB085iB11p06248

Brouard, B., Bérest, P., Djizanne, H., & Frangi, A. (2012). Mechanical stability of a salt cavern submitted to high-frequency cycles. In P. Bérest, M. Ghoreychi, F. Hadj-Hassen, & M. Tijani (Eds.), *The mechanical behavior of salt VII* (pp. 381–390). Paris, France: Taylor & Francis Group.

Carter, N. L., & Hansen, F. D. (1983). Creep of rocksalt. *Tectonophysics*, *92*, 275–333. https://doi.org/10.1016/0040-1951(83)90200-7

Carter, N. L., & Kirby, S. H. (1978). Transient creep and semibrittle behavior of crystalline rocks. *Pure and Applied Geophysics*, *116*, 807–839. https://doi.org/10.1007/BF00876540

Chester, F. M. (1988). The brittle-ductile transition in a deformation-mechanism map for halite. *Tectonophysics*, *154*(1), 125–136. https://doi.org/10.1016/0040-1951(88)90230-2

Chester, F. M. (1988a). *The transition from cataclasis to intracrystalline plasticity in experimental shear zones* (Doctoral dissertation). College Station, TX: Texas A&M University. Retrieved from https://hdl.handle.net/1969.1/DISSERTATIONS-771512

Chester, F. M. (1989b). Dynamic recrystallization in semi-brittle faults. *Journal of Structural Geology*, *11*(7), 847–858. https://doi.org/10.1016/0191-8141(89)90102-8.

Chester, F. M., & Logan, J. (1990). *Frictional faulting in polycrystalline halite: Correlation of microstructure, mechanisms of slip, and constitutive behaviour*. In A. G. Duba, W. B. Durham, J. W. Handin, & H. F. Wang (Eds.), The brittle-ductile transition in rocks: The heard volume (Geophysical Monograph Series, 56, pp. 49–65). Washington, DC: American Geophysical Union. https://doi.org/10.1029/GM056p0049

Coble, C., French, M., Chester, F., Chester, J., & Kitajima, H. (2014). In situ frictional properties of San Andreas Fault gouge at SAFOD. *Geophysical Journal International*, *199*(2), 956–967. https://doi.org/10.1093/gji/ggu306

Dieterich, J. H. (1978). Time-dependent friction and the mechanics of stick-slip. *Pure and Applied Geophysics*, *116*(4), 790–806. https://doi.org/10.1007/BF00876539

Ding, J. (2019). *Grain boundary and elastic behavior in semi-brittle synthetic salt-rock* (Doctoral dissertation). College Station, TX: Texas A&M University. Retrieved from http://hdl.handle.net/1969.1/184425

Ding, J., Chester, F. M., & Chester, J. S. (2017). *Microcrack network development in salt-rock during cyclic loading at low confining pressure*. Paper presented at 51st U.S. Rock Mechanics/Geomechanics Symposium, American Rock Mechanics Association, San Francisco, CA.

Ding, J., Chester, F. M., Chester, J. S., Zhu, C., & Arson, C. (2016). *Mechanical behavior and microstructure development in consolidation of nominally dry granular salt*. Paper presented at 50th U.S. Rock Mechanics/Geomechanics Symposium, American Rock Mechanics Association, Houston, TX.

Ellis, S., & Stöckhert, B. (2004). Elevated stresses and creep rates beneath the brittle-ductile transition caused by seismic faulting in the upper crust. *Journal of Geophysical Research*, *109*(B5), B05407. https://doi.org/10.1029/2003jb002744

Erdogan, F., & Sih, G. C. (1963). On the crack extension in plates under plane loading and transverse shear. *Journal of Basic Engineering*, *85*(4), 519–525. https://doi.org/10.1115/1.3656897

Fokker, P. A. (1995). *The behaviour of salt and salt caverns, (Doctoral dissertation)*. Delft, The Netherlands: Delft University of Technology. Retrieved from http://resolver.tudelft.nl/uuid:6847f8e4-3b09-4787-be02-bcce9f0eed06

Fredrich, J. T., Evans, B., & Wong, T. F. (1989). Micromechanics of the brittle to plastic transition in Carrara marble. *Journal of Geophysical Research*, *94*, 4129–4145. https://doi.org/10.1029/JB094iB04p04129

French, M. E., Chester, F. M., & Chester, J. S. (2015). Micromechanisms of creep in clay-rich gouge from the Central Deforming Zone of the San Andreas Fault. *Journal of Geophysical Research: Solid Earth*, *120*, 827–849. https://doi.org/10.1002/2014JB011496

Frost, H. J., & Ashby, M. F. (1982). *Deformation mechanism maps: The plasticity and creep of metals and ceramics*. Oxford, UK: Pergamon Press.

Fusseis, F., & Handy, M. R. (2008). Micromechanisms of shear zone propagation at the brittle–viscous transition. *Journal of Structural Geology*, *30*(10), 1242–1253. https://doi.org/10.1016/j.jsg.2008.06.005

Griffith, A. (1924). The theory of rupture. In C. B. Biereno, J. M. Burgers, & J. Waltman (Eds.), *Proceedings of the First International Congress on Applied Mechanic* (pp. 54–63). Delft, The Netherlands: Tech. Boekhandel en Drukkerij.

Haupt, M. (1991). A constitutive law for rock salt based on creep and relaxation tests. *Rock Mechanics and Rock Engineering*, *24*(4), 179–206. https://doi.org/10.1007/BF01045031

Hirth, G., & Tullis, J. (1994). The brittle-plastic transition in experimentally deformed quartz aggregates. *Journal of Geophysical Research*, *99*(B6), 11731–11747. https://doi.org/10.1029/93jb02873

Hunsche, U., & Hampel, A. (1999). Rock salt—The mechanical properties of the host rock material for a radioactive waste repository. *Engineering Geology*, *52*(3), 271–291. https://doi.org/10.1016/S0013-7952(99)00011-3

Ivins, E. R. (1996). Transient creep of a composite lower crust: 2. A polymineralic basis for rapidly evolving postseismic deformation modes. *Journal of Geophysical Research*, *101*(B12), 28005–28028. https://doi.org/10.1029/96jb02846

Kirby, S. H. (1980). Tectonic stresses in the lithosphere: Constraints provided by the experimental deformation of rocks. *Journal of Geophysical Research*, *85*, 6353–6363. https://doi.org/10.1029/JB085iB11p06353

Kitajima, H., Chester, F. M., & Biscontin, G. (2012). Mechanical and hydraulic properties of Nankai accretionary prism sediments: Effect of stress path. *Geochemistry, Geophysics, Geosystems*, *13*(10), Q0AD27https://doi.org/10.1029/2012GC004124

Knipe, R. J. (1989). Deformation mechanisms—Recognition from natural tectonites. *Journal of Structural Geology*, *11*, 127–146. https://doi.org/10.1016/0191-8141(89)90039-4

Kohlstedt, D. L., Evans, B., & Mackwell, S. J. (1995). Strength of the lithosphere: Constraints imposed by laboratory experiments. *Journal of Geophysical Research*, *100*, 17587–17602. https://doi.org/10.1029/95JB01460

Mancktelow, N., & Pennacchioni, G. (2020). Intermittent fracturing in the middle continental crust as evidence for transient switching of principal stress axes associated with the subduction zone earthquake cycle. *Geology*, *48*, 1072–1076. https://doi.org/10.1130/g47625.1

Marone, C. (1998). Laboratory-derived friction laws and their application to seismic faulting. *Annual Review of Earth and Planetary Sciences*, *26*(1), 643–696. https://doi.org/10.1146/annurev.earth.26.1.643

Matysiak, A. K., & Trepmann, C. A. (2012). Crystal–plastic deformation and recrystallization of peridotite controlled by the seismic cycle. *Tectonophysics*, *530–531*, 111–127. https://doi.org/10.1016/j.tecto.2011.11.029

Melosh, B. L., Rowe, C. D., Gerbi, C., Smit, L., & Macey, P. (2018). Seismic cycle feedbacks in a mid-crustal shear zone. *Journal of Structural Geology*, *112*, 95–111. https://doi.org/10.1016/j.jsg.2018.04.004

Noda, H., & Shimamoto, T. (2010). A rate- and state-dependent ductile flow law of polycrystalline halite under large shear strain and implications for transition to brittle deformation. *Geophysical Research Letters*, *37*, L09310. https://doi.org/10.1029/2010GL042512

Noda, H., & Shimamoto, T. (2012). Transient behavior and stability analyses of halite shear zones with an empirical rate-and-state friction to flow law. *Journal of Structural Geology*, *38*, 234–242. https://doi.org/10.1016/j.jsg.2011.08.012

Noda, H., & Takahashi, M. (2016). The effective stress law at a brittle-plastic transition with a halite gouge layer. *Geophysical Research Letters*, *43*(5), 1966–1972. https://doi.org/10.1002/2015GL067544

Nüchter, J., & Stöckhert, B. (2008). Coupled stress and pore fluid pressure changes in the middle crust: Vein record of coseismic loading and postseismic stress relaxation. *Tectonics*, *27*(1), TC1007. https://doi.org/10.1029/2007TC002180

Paterson, M. S., & Wong, T.-f. (2005). *Experimental rock deformation-the brittle field* (2nd ed.). Berlin, Germany: Springer-Verlag Berlin Heidelberg.

Peach, C. J., & Spiers, C. J. (1996). Influence of crystal plastic deformation on dilatancy and permeability development in synthetic salt rock. *Tectonophysics*, *256*, 101–128. https://doi.org/10.1016/0040-1951(95)00170-0

Pec, M., Stünitz, H., & Heilbronner, R. (2012). Semi-brittle deformation of granitoid gouges in shear experiments at elevated pressures and temperatures. *Journal of Structural Geology*, *38*, 200–221. https://doi.org/10.1016/j.jsg.2011.09.001

Pec, M., Stünitz, H., Heilbronner, R., & Drury, M. (2016). Semi-brittle flow of granitoid fault rocks in experiments. *Journal of Geophysical Research: Solid Earth*, *121*, 1677–1705. https://doi.org/10.1002/2015JB012513

Pennock, G. M., Drury, M. R., Peach, C. J., & Spiers, C. J. (2006). The influence of water on deformation microstructures and textures in synthetic NaCl measured using EBSD. *Journal of Structural Geology*, *28*, 588–601. https://doi.org/10.1016/j.jsg.2006.01.014

Popp, T., & Kern, H. (2000). Monitoring the state of microfracturing in rock salt during deformation by combined measurements of permeability and P-and S-wave velocities. *Physics and Chemistry of the Earth, Part A: Solid Earth and Geodesy*, *25*(2), 149–154. https://doi.org/10.1016/S1464-1895(00)00024-7

Popp, T., Kern, H., & Schulze, O. (2001). Evolution of dilatancy and permeability in rock salt during hydrostatic compaction and triaxial deformation. *Journal of Geophysical Research*, *106*(B3), 4061–4078. https://doi.org/10.1029/2000jb900381

Raj, R., & Ashby, M. F. (1971). On grain boundary sliding and diffusional creep. *Metallurgical Transactions*, *2*, 1113–1127. https://doi.org/10.1007/BF02664244

Reber, J. E., & Pec, M. (2018). Comparison of brittle- and viscous creep in quartzites: Implications for semi-brittle flow of rocks. *Journal of Structural Geology*, *113*, 90–99. https://doi.org/10.1016/j.jsg.2018.05.022

Roedder, E. (1984). The fluids in salt. *American Mineralogist*, *69*, 413–439.

Rutter, E. H., Atkinson, B. K., & Mainprice, D. H. (1978). On the use of the stress relaxation testing method in studies of the mechanical behaviour of geological materials. *Geophysical Journal of the Royal Astronomical Society*, *55*, 155–170. https://doi.org/10.1111/j.1365-246X.1978.tb04754.x

Scholz, C. H. (2019). *The mechanics of earthquakes and faulting*. Cambridge, UK: Cambridge University Press.

Senseny, P. E., Hansen, F. D., Russell, J. E., Carter, N. L., & Handin, J. W. (1992). Mechanical behavior of rock salt: Phenomenology and micromechanisms. *International Journal of Rock Mechanics and Mining Sciences*, *29*, 363–378. https://doi.org/10.1016/0148-9062(92)90513-Y

Shen, X., & Arson, C. (2019a). An isotropic self-consistent homogenization scheme for chemo-mechanical healing driven by pressure solution in halite. *International Journal of Solids and Structures*, *161*, 96–110. https://doi.org/10.1016/j.ijsolstr.2018.11.010

Shen, X., & Arson, C. (2019b). Simulation of salt-cavity healing based on a micro–macro model of pressure solution. *Petroleum Geoscience*, *25*(3), 251–257. https://doi.org/10.1144/petgeo2018-094

Shen, X., Arson, C., Ding, J., Chester, F. M., & Chester, J. S. (2020). Mechanisms of anisotropy in salt rock upon microcrack propagation. *Rock Mechanics and Rock Engineering*, *53*(7), 3185–3205. https://doi.org/10.1007/s00603-020-02096-1

Shen, X., Ding, J., Arson, C., Chester, J. S., & Chester, F. M. (2021). Micromechanical modeling for rate-dependent behavior of salt rock under cyclic loading. *International Journal for Numerical and Analytical Methods in Geomechanics*, *45*(1), 28–44. https://doi.org/10.1002/nag.3133

Shen, X., Ding, J., Lordkipanidze, I., Arson, C., Chester, J. S., & Chester, F. M. (2021). Fabric evolution and crack propagation in salt during consolidation and cyclic compression tests. *Acta Geotechnica*. https://doi.org/10.1007/s11440-020-01117-1

Shimamoto, T. (1986). Transition between frictional slip and ductile flow for halite shear zones at room temperature. *Science*, *231*(4739), 711–714. https://doi.org/10.1126/science.231.4739.711

Shimamoto, T. (1989). The origin of S-C mylonites and a new fault-zone model. *Journal of Structural Geology*, *11*(1), 51–64. https://doi.org/10.1016/0191-8141(89)90035-7

Shimamoto, T., & Noda, H. (2014). A friction to flow constitutive law and its application to a 2-D modeling of earthquakes. *Journal of Geophysical Research: Solid Earth*, *119*(11), 8089–8106. https://doi.org/10.1002/2014JB011170

Sibson, R. H. (1977). Fault rocks and fault mechanisms. *Journal of the Geological Society*, *133*, 191–213. https://doi.org/10.1144/gsjgs.133.3.0191

Sibson, R. H. (1983). Continental fault structure and the shallow earthquake source. *Journal of the Geological Society*, *140*, 741–767. https://doi.org/10.1144/gsjgs.140.5.0741

Sibson, R. H. (1986). Earthquakes and rock deformation in crustal fault zones. *Annual Review of Earth and Planetary Sciences*, *14*, 149–175. https://doi.org/10.1146/annurev.ea.14.050186.001053

Spiers, C. J., & Carter, N. L. (1996). Micorophysics of rocksalt flow in nature. In M. Aubertin, & H. R. J. Hardy (Eds.), *Proceedings of the Conference on the Mechanical Behavior of Salt IV* (pp. 115–128). Clausthal-Zellerfeld, Germany: Trans Tech Publications.

Spiers, C. J., Schutjens, P. M. T. M., Brzesowsky, R. H., Peach, C. J., Liezenberg, J. L., & Zwart, H. J. (1990). Experimental determination of constitutive parameters governing creep of rocksalt by pressure solution. *Geological Society, London, Special Publications*, *54*, 215–227. https://doi.org/10.1144/GSL.SP.1990.054.01.21

Spiers, C. J., Urai, J. L., Lister, G. S., Boland, J. N., & Zwart, H. J. (1986). *The influence of fluid-rock interaction on the rheology of salt rock*. Luxembourg: Commission of the European Communities.

Stewart, M., Holdsworth, R. E., & Strachan, R. A. (2000). Deformation processes and weakening mechanisms within the frictional–viscous transition zone of major crustal-scale faults: Insights from the Great Glen Fault Zone, Scotland. *Journal of Structural Geology*, *22*(5), 543–560. https://doi.org/10.1016/S0191-8141(99)00164-9

Strehlau, J. (1986). A discussion of the depth extent of rupture in large continental earthquakes. In S. Das J. Boatwright & C. H. Scholz Earthquake source mechanics. Geophysical Monograph Series (Vol. 37, pp. 131–146). Washington, DC: American Geophysical Union. https://doi.org/10.1029/GM037p0131

Ter Heege, J. H., De Bresser, J. H. P., & Spiers, C. J. (2005). Rheological behaviour of synthetic rocksalt: The interplay between water, dynamic recrystallization and deformation mechanisms. *Journal of Structural Geology*, *27*, 948–963. https://doi.org/10.1016/j.jsg.2005.04.008

Tullis, J. A. (1979). High temperature deformation of rocks and minerals. *Reviews of Geophysics*, *17*, 1137–1154. https://doi.org/10.1029/RG017i006p01137

Urai, J. L., Spiers, C. J., Zwart, H. J., & Lister, G. S. (1986). Weakening of rock salt by water during long-term creep. *Nature*, *324*, 554–557. https://doi.org/10.1038/324554a0

Wang, T., Ma, H. L., Shi, X. L., Yang, C. H., Zhang, N., Li, J. L., et al. (2018). Salt cavern gas storage in an ultra-deep formation in Hubei, China. *International Journal of Rock Mechanics and Mining Sciences*, *102*, 57–70. https://doi.org/10.1016/j.ijrmms.2017.12.001

Watanabe, T., & Peach, C. J. (2002). Electrical impedance measurement of plastically deforming halite rocks at 125°C and 50 MPa. *Journal of Geophysical Research*, *107*(B1), 2004–. https://doi.org/10.1029/2001JB000204

Wehrens, P., Berger, A., Peters, M., Spillmann, T., & Herwegh, M. (2016). Deformation at the frictional-viscous transition: Evidence for cycles of fluid-assisted embrittlement and ductile deformation in the granitoid crust. *Tectonophysics*, *693*, 66–84. https://doi.org/10.1016/j.tecto.2016.10.022

White, J. C., & White, S. H. (1983). Semi-brittle deformation within the Alpine fault zone, New Zealand. *Journal of Structural Geology*, *5*(6), 579–589. https://doi.org/10.1016/0191-8141(83)90070-6

Zhang, X., Grupa, J., Spiers, C. J., & Peach, C. J. (2007). Stress relaxation experiments on compacted granular salt. In M. Wallner, K.-H. Lux, W. Minkley, & H. R. J. Hardy (Eds.), *The mechanical behavior of salt VI—Understanding of THMC processes in salt* (pp. 159–166). Paris, France: Taylor & Francis Group.

Zulauf, G. (2001). Structural style, deformation mechanisms and paleodifferential stress along an exposed crustal section: Constraints on the rheology of quartzofeldspathic rocks at supra- and infrastructural levels (Bohemian Massif). *Tectonophysics*, *332*(1), 211–237. https://doi.org/10.1016/S0040-1951(00)00258-4